

THE PHOTOSPHERIC ENERGY AND HELICITY BUDGETS OF THE FLUX-INJECTION HYPOTHESIS

P. W. Schuck[†]

NASA Goddard Space Flight Center

Room 250, Building 21 Space Weather Laboratory, Code 674 Heliophysics Science Division 8801 Greenbelt Rd. Greenbelt, MD 20771, USA

ABSTRACT

The flux-injection hypothesis for driving coronal mass ejections (CMEs) requires the transport of substantial magnetic energy and helicity flux through the photosphere concomitant with the eruption. Under the magnetohydrodynamics approximation, these fluxes are produced by twisting magnetic field and/or flux emergence in the photosphere. A CME trajectory, observed 2000 September 12 and fitted with a flux-rope model constrains energy and helicity budgets for testing the flux-injection hypothesis. Optimal velocity profiles for several driving scenarios are estimated by minimizing the photospheric plasma velocities for a cylindrically symmetric flux-rope magnetic field subject to the flux budgets required by the flux-rope model. Ideal flux injection, involving only flux emergence, requires hypersonic upflows in excess of the solar escape velocity 617 km s^{-1} over an area of $6 \times 10^8 \text{ km}^2$ to satisfy the energy and helicity budgets of the flux-rope model. These estimates are compared with magnetic field and Doppler measurements from *Solar Heliospheric Observatory*/Michelson Doppler Imager on 2000 September 12 at the footpoints of the CME. The observed Doppler signatures are insufficient to account for the required energy and helicity budgets of the flux-injection hypothesis.

Subject headings: Sun: coronal mass ejections - Sun: photosphere - Sun: surface magnetism

1. INTRODUCTION

Over the last 10 years, the flux-rope model developed by Chen (1989, 1996) has been used to describe the dynamics of coronal mass ejections (CMEs) observed by the Large Angle Spectrometric Coronagraphs (LASCO) aboard the *Solar and Heliospheric Observatory*¹ (*SOHO*) (Chen et al. 1997, 2000; Wood et al. 1999; Krall et al. 2001; Chen et al. 2006; Krall et al. 2006). However, the photospheric flux injection paradigm used to initiate and drive the eruption has been criticized because the surge of electromagnetic energy flowing through the photosphere is “difficult to reconcile with the extremely tranquil conditions that exist during flares and CMEs” (Forbes 2000, 2001; Rust 2001). Chen et al. (2000), Chen (2001), Krall et al. (2001), Chen & Krall (2003) and Chen & Kunkel (2010) have attempted to address these criticisms and a previous study has examined the implications of uniformly twisting to coronal footpoints of the flux rope (Krall et al.

[†]peter.schuck@nasa.gov

¹*SOHO* is a project of international cooperation between ESA and NASA.

2000). However, no quantitative comparisons between flux-injection hypothesis and detailed photospheric observations have been considered by the formal literature.

The goal of this paper is to provide a framework for testing the flux-injection hypothesis through the photospheric signatures implied by the energy and helicity budgets of CMEs described by the flux-rope model. The paper is organized as follows: Section 2 describes the flux-rope model of Chen (1989) and a simple extension of the flux-rope model magnetic field into the photosphere.

Section 3 develops the photospheric fluxes necessary to satisfy the energy and helicity budgets of CMEs fitted with the flux-rope model. The photospheric magnetic field combined with the photospheric fluxes is used to estimate minimum velocities necessary to satisfy the energy and helicity budgets required by CME trajectories fitted by the flux-rope model under the flux-injection hypothesis. Two examples of CME trajectories fitted with the flux-rope model are used to constrain the photospheric velocities. 1) The first event is the 2000 September 12 CME that erupted from decaying NOAA active region 9163. The height-time data for the CME trajectory (Chen et al. 2006) were derived from measurements of the filament in absorption observed by the Global H α Network at Kanzelhöhe Solar Observatory (KSO) in Austria (Steinegger et al. 2000), and LASCO C2 and C3 observations of the filament in emission (Brueckner et al. 1995). Complementary observations of the filament were made in Fe XII 195 Å by the *SOHO*/EUV Imaging Telescope (EIT) instrument (Delaboudinière et al. 1995). The eruption occurred shortly after 11:30 UT and the filament first appeared in LASCO C2 at 12:30 UT. This CME was associated with an M1.0 class flare with distinct flare ribbons that persisted for 2 hr. Various aspects of this event, such as morphology, timing, and reconnection rate have been discussed by Vršnak et al. (2003), Schuck et al. (2004b) and Qiu et al. (2004). 2) The second event is the 2003 October 28 CME which originated from large complex NOAA active region 10468 at about 11:00 UT. The event was extremely fast, and thus the height-time data for the leading edge of the CME consists of only one LASCO C2 image at about 11:30 UT and four subsequent LASCO C3 images. This event was associated with an extremely powerful X17 flare and consequently has received extensive attention in the literature (Seppälä et al. 2004; Skoug et al. 2004; Woods et al. 2004; Zurbuchen et al. 2004; Bieber et al. 2005; Chi et al. 2005; Degenstein et al. 2005; Hu et al. 2005; Gopalswamy et al. 2005; Looper et al. 2005; Pallamraju & Chakrabarti 2005; Tsurutani et al. 2005; Yurchyshyn et al. 2005; Krall et al. 2006; Manchester et al. 2008).

Section 4 compares the photospheric velocities implied by the flux-rope CME trajectory event from 2000 September 12, against detailed photospheric Doppler measurements from the Michelson Doppler Imager (MDI) aboard *SOHO* (Scherrer et al. 1995). Finally, Section 5 compares these theoretical results and Doppler observations with previous work.

2. THE FLUX-ROPE MODEL

Figure 1 shows a schematic diagram of the flux-rope CME model current loop, adapted from Chen (1989, 1996). Shafranov (1966) derived the magnetohydrodynamic (MHD) forces per-unit-length acting the major \mathcal{R} and minor a radii of a current carrying toroidal section

$$f_R \equiv \frac{I_\phi^2}{c^2 \mathcal{R}} \left[\ln \left(\frac{8 \mathcal{R}}{a} \right) + \frac{\Delta\beta}{2} - \frac{\langle B_\phi \rangle^2}{2 B_{\theta a}^2} + \frac{2 \mathcal{R}}{a} \frac{B_c}{B_{\theta a}} - 1 + \frac{\xi}{2} \right], \quad (1a)$$

$$f_a \equiv \frac{I_\phi^2}{c^2 a} \left(\frac{\langle B_\phi \rangle^2}{B_{\theta a}^2} - 1 + \Delta\beta \right), \quad (1b)$$

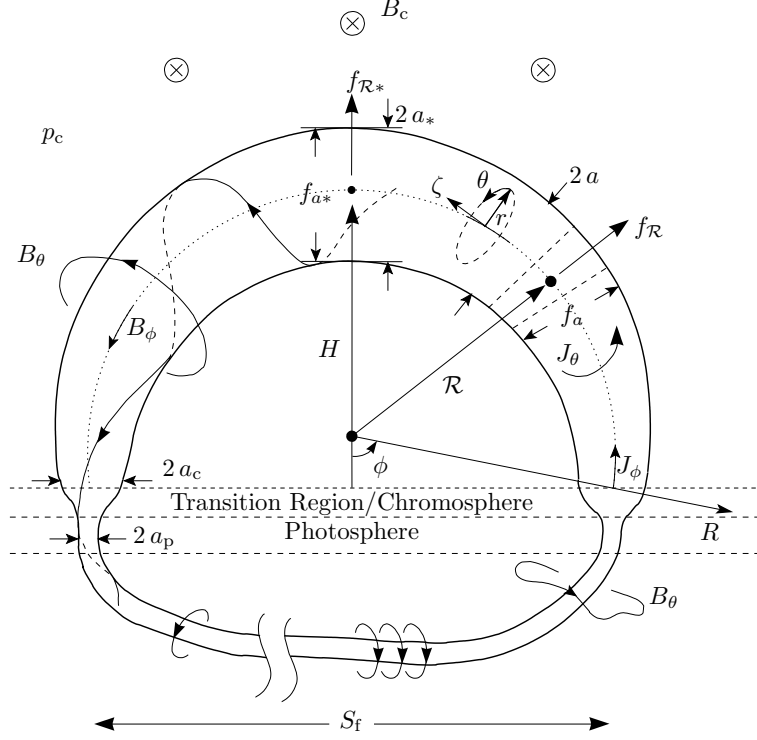


Fig. 1.— Schematic diagram of the flux-rope model current loop adapted from Chen (1989, 1996). The subscripts “ ϕ ” and “ θ ” refer to the toroidal and poloidal directions in the cylindrical (R, ϕ, Z) and the local polar (r, θ, ζ) coordinate systems for a circular torus where \hat{Z} is out of the plane of the page.

where I_ϕ is the toroidal current, c is the speed of light, $\langle B_\phi \rangle$ is the average toroidal field inside the current channel, B_c is a prescribed function describing the overlying coronal field perpendicular to the flux rope, $B_{\theta a} \equiv B_\theta(a) = 2I_\phi/ac$ is the poloidal magnetic field at the edge of the current channel, and

$$\xi \equiv \frac{2 \int_0^a dr r B_\theta^2(r)}{a^2 B_{\theta a}^2} = \frac{c^2}{2I_\phi^2} \int_0^a dr r B_\theta^2(r) \sim \mathcal{O}(1), \quad (2)$$

is the internal inductance. The quantity $\Delta\beta \equiv 8\pi(\langle p \rangle - p_c)/B_{\theta a}^2$ is the differential of plasma β based on $B_{\theta a}$ where $\langle p \rangle$ is the average internal flux-rope pressure and p_c is the coronal pressure. The subscripts “ ϕ ” and “ θ ” refer to the toroidal and poloidal directions in the cylindrical (R, ϕ, Z) and the local polar (r, θ, ζ) coordinate systems for a circular torus with $R = \mathcal{R} + r \cos\theta$, $Z = r \sin\theta$ and $\hat{\zeta} = \hat{\phi}$ where \hat{Z} is out of the plane of the page. Chen (1989) applied Equation (1) at the peak of the flux rope to derive the dynamical equations

$$M \frac{d^2 H}{dt^2} = \frac{I_\phi^2}{c^2 \mathcal{R}} \left[\ln \left(\frac{8 \mathcal{R}}{a_*} \right) + \frac{\Delta\beta_*}{2} - \frac{\langle B_{\phi_*} \rangle^2}{2 B_{\theta a_*}^2} + \frac{2 \mathcal{R}}{a_*} \frac{B_c}{B_{\theta a_*}} - 1 + \frac{\xi_*}{2} \right] + f_d + f_g, \quad (3a)$$

and

$$M \frac{d^2 a_*}{dt^2} = \frac{I_\phi^2}{c^2 a_*} \left(\frac{\langle B_{\phi_*} \rangle^2}{B_{\theta a_*}^2} - 1 + \Delta\beta_* \right), \quad (3b)$$

where $H > 0$ is the height of the center of the current channel above the photosphere henceforth referred to as the “apex.” The $*$ ’s in Equation (3) denote quantities evaluated over the cross section at the apex where $M \equiv \langle n_* \rangle m \pi a_*^2$ is the mass per-unit-length of the flux rope and $\langle n_* \rangle$ is the average density of the flux rope. The additional terms

$$f_d = c_d n_c m a_* (V_{\text{SW}} - V) |V_{\text{SW}} - V| \quad (4a)$$

and

$$f_g = \pi a_*^2 m g (n_c - \langle n_* \rangle), \quad (4b)$$

introduced in Chen (1989), represent the drag and gravitational forces per-unit-length of the flux rope respectively where $c_d \sim \mathcal{O}(1)$ is the drag coefficient, $m = 1.67 \times 10^{-24}$ g is the mass of hydrogen, n_c is the ambient coronal density, $V \equiv dH/dt$, V_{SW} is the velocity of the ambient solar wind, and the gravitational acceleration is

$$g = \frac{g_\odot}{(1 + H/R_\odot)^2}, \quad (5)$$

with $g_\odot = 2.74 \times 10^4$ cms $^{-1}$ and $R_\odot = 6.74 \times 10^{10}$ cm. The flux-rope footpoints are separated by a distance S_f in the photosphere and assumed to remain fixed throughout the evolution of the flux-rope CME by the “dense subphotospheric plasma” (Chen 1989). The current-channel radius at the base of the corona a_c is also assumed to remain fixed throughout the evolution of the flux rope. The major radius \mathcal{R} and height H above the photosphere are related by

$$\mathcal{R} \equiv \frac{H^2 + S_f^2/4}{2H} \quad \text{and} \quad H > 0. \quad (6)$$

The length of the flux rope above the photosphere is $L = 2\pi\Theta\mathcal{R}$ where

$$\Theta \equiv \begin{cases} 1 - \varphi/\pi & H \geq S_f/2, \\ \varphi/\pi & H < S_f/2, \end{cases} \quad (7)$$

and $\varphi \equiv \arcsin(S_f/2\mathcal{R})$ (Chen 1989; Krall et al. 2000). Note the variables that describe the plasma at the apex of the flux rope $\langle n_* \rangle$, $\langle p_* \rangle$, $B_{\theta a_*}$, B_{ϕ_*} , and I_ϕ will evolve with time and parameters of the interplanetary medium n_c , B_c , and V_{SW} are implicit functions of H . (see Chen 1996, for a complete description of the interrelations between variables and a model for the parameters of the interplanetary medium) (Krall et al. 2000).

Flux-rope equilibria are determined from

$$f_{R*} = f_{a*} = 0. \quad (8)$$

Chen & Garren (1994), Chen (1996), Krall et al. (2000), and Krall & Chen (2005) proposed local polar equilibrium profiles for $\partial_\zeta \approx 0$ and large aspect ratio $\mathcal{R}/a \gg 1$

$$B_\theta(r) = B_{\theta a} \begin{cases} 3 \frac{r}{a} \left(1 - \frac{r^2}{a^2} + \frac{r^4}{3a^4} \right) & r < a, \\ \frac{a}{r} & r > a, \end{cases} \quad (9a)$$

$$B_\phi(r) \simeq B_\zeta(r) = 3 B_{\zeta a} \begin{cases} 1 - 2 \frac{r^2}{a^2} + \frac{r^4}{a^4} & r < a, \\ 0 & r > a, \end{cases} \quad (9b)$$

compatible with the flux-rope model with a toroidal flux of

$$\Phi_\phi = \Phi_\zeta \equiv \langle B_\zeta \rangle \pi a^2 = B_{\zeta a} \pi a^2, \quad (10a)$$

and carrying a bare toroidal current of

$$I_\phi = I_\zeta = B_{\zeta a} a c/2. \quad (10b)$$

There is no return current which is consistent with the large-scale current systems in active regions analyzed by Wheatland (2000). Since Equations (9a) and (9b) do not represent a force-free equilibria $\mathbf{J} \times \mathbf{B} = 0$, the poloidal and toroidal magnetic fields and corresponding currents are decoupled.² Consequently, the cutoff of the toroidal field B_ζ at $r = a$ is arbitrary relative to the poloidal magnetic field. For example,

$$B_\zeta(r) = B_{\zeta a} e^{-r^2/a^2}, \quad (11)$$

is a valid toroidal field model and contains the identical amount of flux as Equation (9b).

The toroidal energy per-unit-length of the flux rope is

$$\mathcal{U}_\zeta = \frac{1}{4} \int_0^a dr r B_\zeta^2(r) \simeq \frac{9}{40} B_{\zeta a}^2 a^2, \quad (12a)$$

and the poloidal energy per unit length contained within a distance of radius r of the toroidal axis of the flux rope is

$$\mathcal{U}_\theta(r) = \frac{1}{4} \int_0^r dr' r' B_\theta^2(r') \simeq \frac{B_{\theta a}^2 a^2}{480} [73 + 120 \log(r_c/a)]. \quad (12b)$$

The local polar equilibrium profile Equations (9a) and (9b) does not formally admit a bounded poloidal energy per unit length along the flux rope—a necessary physical condition for admissibility—because $B_\theta \sim r^{-1}$ and $\mathcal{U}_\theta(r) \sim \log(r)$ for $r > a$. However, for the closed circuit representative of the schematic flux rope shown in Figure 1, the integral is cutoff at distances of order of the dimension of the circuit (see pp. 136-141 in Landau & Lifshitz 1960) which is roughly half the footpoint separation $r_c \simeq S_f/2$. The fraction of poloidal magnetic energy contained inside radius r is then

$$\delta_\theta(r, a, r_c) \equiv \frac{\mathcal{U}_\theta(r)}{\mathcal{U}_\theta(r_c)} \simeq \frac{73 + 120 \log(r/a)}{73 + 120 \log(r_c/a)}. \quad (13)$$

Chen et al. (2000) have argued that a “large fraction of the injected poloidal energy is in the magnetic field outside the current channel,” denoted by $r = a$. Indeed, in the corona, roughly 1/3 of poloidal energy is contained within the current channel $r \leq a$. However, more than 2/3 of the poloidal energy is contained within the region $r \leq 2a$ near the current channel. In the photosphere, the amounts are reduced because the current channel is narrower, but the poloidal energy is contained within the region $r \leq 2a$ near where the current channel remains significant varying from $1/3 \Rightarrow 2/3$ depending on the strength of the toroidal field in the photosphere. The comparison of the flux-injection hypothesis against photospheric observations in Section 4 is limited to the region $r \leq 2a$ where the poloidal energy transport is substantial and the poloidal magnetic field is significant.

Although the magnetic field model Equations (9a) and (9b) was originally proposed as an approximate local description for large-aspect ratio coronal toroidal flux-rope magnetic fields, it has also been used as an initial equilibrium for investigating photospheric signatures in simulations of subphotospheric flux ropes

²In equilibrium, the magnetic pressure is in detailed balance with gravity and kinetic pressure.

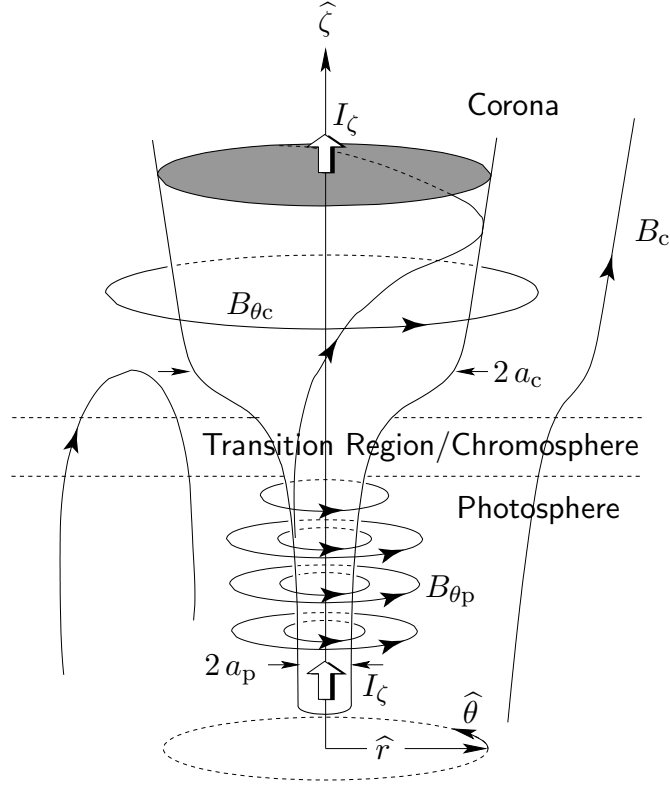


Fig. 2.— Schematic diagram of the flux-rope leg through the photosphere adapted from Chen (2001). The current channel carrying I_ζ , the top of which is shaded, and the poloidal field B_θ , and two community field lines extending into the corona B_c are shown. The subscripts “c” and “p” refer to coronal and photospheric values respectively.

(Chen & Huba 2005a,b, 2006) and similar models have been implemented for modeling the photosphere flux-rope dynamics (Sakai et al. 2000; Sakai et al. 2001). Figure 2 shows a schematic diagram of the flux-rope leg through the photosphere adapted from Chen (2001) in the local polar r, θ, ζ coordinate system. The vertical current channel carrying I_ζ , the top of which is shaded, and the private poloidal field B_θ , and two community field lines extending into the corona B_c are shown. The subscripts “c” and “p” refer to values at the base of the corona and in the photosphere, respectively. Two general constraints may be applied quasi-adiabatically to extend the coronal model into the photosphere: conservation of vertical flux and vertical current (Krall & Chen 2005)

$$B_{\zeta p} = B_{\zeta c} \frac{a_c^2}{a_p^2}, \quad (14a)$$

$$B_{\theta p} = B_{\theta c} \frac{a_c}{a_p}. \quad (14b)$$

Combining these relationships with Equations (9a) and (9b) produces an approximate local model for the magnetic footpoints of the flux rope in the photosphere with $B_{\zeta c} = B_{\phi c}$ at the base of the corona. The details of the flux-tube expansion in the chromosphere is not explicitly specified in this approximation. However, the expansion implies a local radial field $B_r(r)$ to balance the decrease of $B_\zeta(\zeta)$ with height under the local

constraint of $\nabla \cdot \mathbf{B} = 0$.

3. THE PHOTOSPHERIC FLUX BUDGETS OF THE FLUX-ROPE MODEL

The flux-rope model requires specification of two quantities in addition to the geometrical aspects of the flux rope, namely the toroidal and poloidal fluxes (Chen 1996)

$$\Phi_\phi = B_{\phi c} \pi a_c^2 = \text{constant}, \quad (15a)$$

$$\Phi_\theta = c \mathcal{L} I_\phi, \quad (15b)$$

where

$$\mathcal{L} \simeq \frac{4\pi\Theta\mathcal{R}}{c^2} \left\{ \log(8\mathcal{R}) - 1 + \frac{\xi}{2} - \frac{1}{a_* - a_c} [a_* \log(a_*) - a_c \log(a_c)] \right\} \quad (16)$$

is the inductance (Landau & Lifshitz 1960; Krall et al. 2000). The toroidal energy is estimated from the arclength of the flux rope above the photosphere.³

$$U_\phi \simeq \frac{9\pi\Theta}{20} \frac{\mathcal{R}}{a_*} B_{\phi a_c}^2 a_c^3 = \frac{9\Theta}{20\pi} \frac{\Phi_\phi^2}{a_c} \frac{\mathcal{R}}{a_*} \approx \text{constant}, \quad (17a)$$

whereas the poloidal energy is related to the inductance and poloidal flux

$$U_\theta = \frac{1}{2} \mathcal{L} I_\phi^2 = \frac{1}{2c^2} \frac{\Phi_\theta^2}{\mathcal{L}}. \quad (17b)$$

The toroidal flux $\Phi_\phi = \Phi_\zeta$ is conserved because the toroidal field $B_{\phi a_c} = B_{\zeta a_c}$ and current-channel radius a_c at the base of the corona are held constant in time during the eruption— $B_{\phi a}$ and the minor radius a may vary along the flux rope subject to flux conservation. The toroidal energy U_ϕ is conserved because the flux rope erupts self-similarly $\mathcal{R}/a_* \approx \text{constant}$. Consequently, the quantities that will manifest dynamical changes in the photosphere during the eruption are the poloidal power dU_θ/dt and the rate-of-change in poloidal flux $d\Phi_\theta/dt$ which are related to the photospheric energy and helicity fluxes respectively.

The MHD induction equation derived by combining Faraday's Law

$$\partial_t \mathbf{B} = -c \nabla \times \mathbf{E}, \quad (18)$$

with Ohm's Law

$$\mathbf{E} = \frac{\mathbf{J}}{\sigma} - \frac{\mathbf{v}}{c} \times \mathbf{B}, \quad (19)$$

to obtain

$$\partial_t \mathbf{B} = \nabla \times (\mathbf{v} \times \mathbf{B}) - c \nabla \times \left(\frac{\mathbf{J}}{\sigma} \right), \quad (20)$$

where \mathbf{v} is the plasma velocity and σ is a spatially variable conductivity. The magnetic energy in the corona is formulated by dotting the induction Equation (20) with the magnetic field \mathbf{B} and using Ampere's Law without displacement currents

$$\nabla \times \mathbf{B} = \frac{4\pi}{c} \mathbf{J}, \quad (21)$$

³The flux-rope minor current-channel radius varies linearly with arc length $a(\ell) = a_c + (a_* - a_c) \ell$ from the footpoint at $\ell = 0$ to the apex at $\ell = 1$.

to derive Poynting theorem

$$\frac{dU_M}{dt} \equiv \frac{d}{dt} \int_{V_c} \frac{dV}{8\pi} B^2 = \frac{1}{4\pi} \oint_S dS \hat{n} \cdot \left[\mathbf{B} \times (\mathbf{v} \times \mathbf{B}) + \frac{c}{\sigma} (\mathbf{J} \times \mathbf{B}) \right] - \int_{V_c} dV \left[\frac{\mathbf{v}}{c} \cdot (\mathbf{J} \times \mathbf{B}) + \frac{J^2}{\sigma} \right], \quad (22)$$

where the volume integrals V_c are over the corona, chromosphere, and transition region, the surface integrals bounding the volume $S \equiv S_p + S_{oc}$ are over the photosphere S_p and the outer corona S_{oc} at $R \gg R_\odot$, and \hat{n} is the surface normal pointing into the coronal volume (radially outward at the photosphere S_p and radially inward at the outer corona S_{oc}). Assessing the energy budget of the region between the photosphere and outer corona by tracking the Poynting flux through the photosphere and the energy leaving the corona through eruptive phenomena provides an estimate for the free energy available for producing flares and CMEs (see Figure 1 in Kusano et al. 2002). The first and second terms in Equation (22) represent the $\mathbf{E} \times \mathbf{B}$ Poynting flux through the surfaces and the third and fourth terms represent the conversion of magnetic energy to kinetic energy through work done by the $\mathbf{J} \times \mathbf{B}$ force on the plasma and Ohmic heating through resistivity respectively.

The helicity for the flux rope may be written⁴ (Chen 1996; Chen & Krall 2003)

$$K \equiv \int_{V_c} dV \mathbf{A} \cdot \mathbf{B} \simeq \Phi_\phi \Phi_\theta. \quad (23)$$

Comparisons between integrated photospheric helicity flux and the poloidal flux injection profile for the flux-rope model can be made. However, because the field lines of the flux rope penetrate the photosphere, a gauge-invariant *relative* helicity must be used for estimating helicity fluxes through the photosphere (Berger & Field 1984)

$$\Delta K = \int_{V_c} dV (\mathbf{A} \cdot \mathbf{B} - \mathbf{A}_R \cdot \mathbf{B}_R), \quad (24)$$

where V_c corresponds to the volume above the photosphere and $\mathbf{B}_R = \nabla \times \mathbf{A}_R$ are the reference fields which are chosen to match the normal components of \mathbf{B} and the tangential components of \mathbf{A} respectively at the surface:

$$(\mathbf{A} - \mathbf{A}_R) \times \hat{n}|_S = 0, \quad (25a)$$

$$(\mathbf{B} - \mathbf{B}_R) \cdot \hat{n}|_S = 0. \quad (25b)$$

These boundary conditions are sufficient for the equivalence of the relative helicity defined by Berger & Field (1984) in Equation (24) and manifestly gauge invariant relative helicity defined by Finn & Antonsen (1985)

$$\Delta K = \int_{V_c} dV (\mathbf{A} + \mathbf{A}_R) \cdot (\mathbf{B} - \mathbf{B}_R), \quad (26)$$

because

$$\begin{aligned} \int_{V_c} dV (\mathbf{A}_R \cdot \mathbf{B} - \mathbf{A} \cdot \mathbf{B}_R) &= \int_{V_c} dV (\mathbf{A}_R \cdot \nabla \times \mathbf{A} - \mathbf{A} \cdot \nabla \times \mathbf{A}_R), \\ &= \int_{V_c} dV \nabla \cdot (\mathbf{A} \times \mathbf{A}_R), \\ &= - \int_S dS \hat{n} \cdot (\mathbf{A} \times \mathbf{A}_R), \\ &= 0, \end{aligned} \quad (27)$$

⁴See pp. 21,516 in Chen (1996). This expression is exact in the large aspect ratio limit $\mathcal{R}/a \gg 1$.

with Equation (25).

A judicious choice for the reference field is a potential field

$$\mathbf{B}_R = \nabla \times \mathbf{A}_R = \nabla \Psi_R, \quad (28a)$$

in the Coulomb gauge

$$\nabla \cdot \mathbf{A}_R = 0, \quad (28b)$$

with the additional boundary condition

$$\hat{n} \cdot \mathbf{A}_R|_S = 0. \quad (28c)$$

For these conditions, this reference field has zero helicity

$$K_R = \int_{V_c} dV \mathbf{A}_R \cdot \mathbf{B}_R = \int_{V_c} dV \mathbf{A}_R \cdot \nabla \Psi_R = \oint_S dS \hat{n} \cdot \mathbf{A}_R \Psi_R - \int_{V_c} dV \Psi_R \nabla \cdot \mathbf{A}_R = 0. \quad (29)$$

Using Equation (24) or (26) with Equations (28a) and (28b) and boundary conditions (25) and (28c), the Poynting theorem for the magnetic helicity into the corona then takes a particularly simple form

$$\frac{d\Delta K}{dt} = \frac{d}{dt} \int_{V_c} dV \mathbf{A} \cdot \mathbf{B}, \quad (30a)$$

$$= 2 \oint_S dS \hat{n} \cdot [\mathbf{A}_R \times (\mathbf{v} \times \mathbf{B}) - \frac{c}{\sigma} \mathbf{A}_R \times \mathbf{J}] - 2c \int_{V_c} dV \frac{\mathbf{J} \cdot \mathbf{B}}{\sigma}. \quad (30b)$$

The first and second terms in Equation (30b) represent the helicity flux through the photosphere and the third term represents helicity dissipation in the coronal volume.

Although the photosphere is not ideal, with a magnetic Reynolds number of $R_M = UL/\eta \sim 10^5 - 10^6$ where U is the typical velocity, L is the typical gradient scale, and $\eta = c^2/(4\pi\sigma)$ is the magnetic diffusivity, the ideal approximation has been demonstrated to be adequate for inferring plasma velocities from magnetic field dynamics in convection zone simulations⁵ with magnetic Reynolds numbers as low as $R_M \sim 10^3$ (Welsch et al. 2007; Schuck 2008). The ideal MHD induction equation becomes

$$\partial_t \mathbf{B} = \nabla \times (\mathbf{v} \times \mathbf{B}). \quad (31)$$

Within the flux injection paradigm, consistent with Equation (15a), the toroidal magnetic field in the photosphere does not change during the eruption (Chen et al. 1997)

$$\partial_t B_\zeta = \hat{\zeta} \cdot \nabla \times (\mathbf{v} \times \mathbf{B}) \approx 0. \quad (32)$$

This relationship also represents an *observational constraint* on the vertical magnetic field of the flux rope in the photosphere because large changes in line-of-sight magnetograms near disk center have not been observed during eruptions. This constraint on the vertical magnetic field implies

$$\mathbf{v} \times \mathbf{B} \approx \nabla_h \psi + (v_r B_\theta - B_r v_\theta) \hat{\zeta}, \quad (33a)$$

where the subscript “h” refers to the horizontal (r, θ) coordinates of the local polar coordinate system and ψ is the electrostatic potential. Solving Equation (33a) for \mathbf{v} produces

$$\mathbf{v} = \frac{\hat{\zeta} \times \mathbf{B} (\mathbf{B} \cdot \nabla_h \psi)}{B_\zeta B^2} - \frac{\nabla_h \psi \times \mathbf{B}}{B^2} + v_\parallel \mathbf{B} / |\mathbf{B}|, \quad (33b)$$

⁵See Abbett et al. (2004).

where v_{\parallel} is the field-aligned plasma velocity. For a locally cylindrical flux rope with $\partial_{\theta} = 0$ and $B_r = 0$ consistent with Equation (9), the evolution of the radial and poloidal fields at the photosphere are determined by

$$\partial_t B_r = 0, \quad (34a)$$

$$\partial_t B_{\theta} = \partial_{r\zeta} \psi - B_{\zeta}^{-1} (\partial_{\zeta} B_{\zeta}) (\partial_r \psi), \quad (34b)$$

$$\partial_t B_{\zeta} = 0. \quad (34c)$$

Chen (1996) and Chen & Kunkel (2010) have noted that the poloidal magnetic field at the base of the corona may only increase by 20%-50% during the first 30 minutes of the eruptions and Krall et al. (2001) have shown an event that requires no perceptible increase in the poloidal magnetic field (see Figure 8(a) in Krall et al. 2001). To the extent that $\partial_{\zeta} \approx 0$, these results are consistent with MHD.

3.1. The Ideal Poynting Fluxes in the Photosphere

From Equations (22), (30b), and (33b), the ideal MHD energy flux through the photosphere is

$$\begin{aligned} u_{\zeta} &= \frac{1}{4\pi} (v_{\zeta} \mathbf{B}_h - B_{\zeta} \mathbf{v}_h) \cdot \mathbf{B}_h, \\ &= -\frac{1}{4\pi} (\widehat{\zeta} \times \nabla_h \psi) \cdot \mathbf{B}_h, \end{aligned} \quad (35)$$

and the helicity flux is

$$\begin{aligned} k_{\zeta} &= 2 (v_{\zeta} \mathbf{B}_h - B_{\zeta} \mathbf{v}_h) \cdot \mathbf{A}_R, \\ &= 2 \widehat{\zeta} \cdot (\mathbf{A}_R \times \nabla_h \psi). \end{aligned} \quad (36)$$

Equations (33), (34b), (35), and (36) are general with respect to the constraint (32); the fluxes through the photosphere are completely specified by the electric potential ψ and the magnetic field. The flux-injection hypothesis has always appealed to some “unspecified sub-photospheric process” for initiating and driving the CME (Krall et al. 2000; see also Chen 1989; Chen & Garren 1993; Chen 1996; Chen et al. 1997; Chen 1997; Chen et al. 2000; Chen 2001; Chen & Krall 2003; Krall et al. 2001; Chen & Kunkel 2010). Nonetheless, in the ideal MHD limit, energy is transported through the photosphere by the term $\widehat{\zeta} \cdot \mathbf{B} \times (\mathbf{v} \times \mathbf{B})$ and helicity is transported by $\widehat{\zeta} \cdot \mathbf{A}_R \times (\mathbf{v} \times \mathbf{B})$. These terms integrated over the footpoints in the photosphere (including the region outside the current channel) must balance the poloidal power requirements dU_{θ}/dt and helicity requirements $dK/dt \simeq \Phi_{\phi} d\Phi_{\theta}/dt$ of a CME described by the flux-rope model. Temporally, the increase in the fluxes at the footpoints should precede the eruptions by at least $\delta t \simeq 4$ minutes to account for the transport of magnetic field along the flux rope to the apex of the CME at the coronal Alfvén speed⁶ $V_A \simeq 1.5 \times 10^8 \text{ cm s}^{-1}$.

Assuming azimuthal symmetry $\partial_{\theta} = 0$, the poloidal power injected through the flux-rope footpoints can be written in terms of Equation (17b) or (35)

$$\frac{dU_{\theta}}{dt} \simeq \left(\frac{2}{\Phi_{\theta}} \frac{d\Phi_{\theta}}{dt} - \frac{1}{\mathcal{L}} \frac{d\mathcal{L}}{dt} \right) \frac{\Phi_{\theta}^2}{2\mathcal{L}c^2} \simeq -2 \times \frac{1}{2} \int_0^{r_c} dr r B_{\theta} \partial_r \psi = - \int_0^{r_c} dr r B_{\theta} \partial_r \psi, \quad (37)$$

⁶The Alfvén speed is based on flux-rope initial conditions from (Chen 1996) with $\langle n \rangle \simeq 7.5 \times 10^7 \text{ cm}^{-3}$ and $B \simeq 6 \text{ G}$. Note that this estimate is an order of magnitude larger than estimates corresponding to the same height range by Régnier et al. (2008).

and because the toroidal flux is constant, the rate of change of helicity is

$$\frac{dK}{dt} \simeq \Phi_\phi \frac{d\Phi_\theta}{dt} \simeq -2 \times 4\pi \int_0^{r_c} dr r A_{R\theta} \partial_r \psi, \quad (38)$$

where the fluxes are assumed to be equipartitioned between the two footpoints. Equations (37) and (38) represent *independent* constraints between the flux-rope dynamics and the energy and helicity fluxes in the photosphere.

Balancing the photospheric Poynting fluxes against the poloidal energy and helicity budgets of CME trajectories fit by the flux-rope model requires choosing a photospheric model for the magnetic field and a velocity profile or $\partial_r \psi$. For the former, the simple photospheric extension of the flux-rope model described in Section 2 is used. For the latter, the *optimal* velocities for transporting energy and helicity across the photosphere consistent with the respective overall budgets of the flux-rope model are estimated via constrained variational calculus (see Appendices A and B). *Optimal*, in this context, means the *minimum* root-mean-squared (rms) photospheric velocities corresponding to the minimum photospheric kinetic energy (for constant density).

There are two physical mechanisms for transporting energy and helicity through the photosphere and into the corona:

1. Twisting the magnetic field in the photosphere through poloidal motion. Under this mechanism and the magnetic field model in Equation (9), all the energy and helicity must be transported through the photosphere and into the corona within the current channel where $B_\zeta \neq 0$. Minimizing $\int dr r v_\theta^2$ with $v_\zeta = 0$, the rms poloidal photospheric velocity inside $r \leq a_p$ constrained by the energy budget is derived in Appendix A

$$\langle v_\theta^2 \rangle_{a_p}^{1/2} = \left| \frac{dU_\theta}{dt} \right| \frac{4\sqrt{70}}{\sqrt{437} |B_{\theta c}^2 B_{\zeta c}| a_c^2} \frac{1}{\sqrt{|B_{\zeta p}|}} \propto \frac{1}{\sqrt{|B_{\zeta p}|}}, \quad [\text{A10}]$$

and constrained by the helicity budget derived in Appendix B

$$\langle v_\theta^2 \rangle_{a_p}^{1/2} = \left| \frac{d\Phi_\theta}{dt} \right| \sqrt{\frac{70}{437}} \frac{1}{\sqrt{|B_{\zeta c} B_{\zeta p}|}} \frac{1}{a_c}. \quad [\text{B7}]$$

The twisting of footpoints does not change the net current carried by the flux rope (see discussion on pp. 30 and Appendix C).

2. Flux injection involving the emergence of poloidal flux transported through the photosphere by vertical motion. Under this mechanism and the magnetic field model in Equation (9), the energy and helicity transport are not limited to the current channel, but significant transport occurs within about $r \lesssim 2 a_p$. Minimizing $\int dr r v_\zeta^2$ with $v_\theta = 0$, the rms vertical photospheric velocity inside $r \leq 2 a_p$ constrained by the energy budget is derived in Appendix A

$$\langle v_\zeta^2 \rangle_{2 a_p}^{1/2} = \left| \frac{dU_\theta}{dt} \right| \frac{\sqrt{12516735} |B_{\zeta p}| r_c^2}{2 B_{\theta c}^2 a_c^2 |2998 B_{\zeta p} r_c^2 - 1155 B_{\zeta c} a_c^2|}. \quad [\text{A13}]$$

Note that Equation (A13) approaches a constant asymptotically if either $r_c \rightarrow \infty$ or $B_{\zeta p} \rightarrow \infty$, while holding the coronal flux constant $B_{\zeta c} a_c^2$

$$\langle v_\zeta^2 \rangle_{2 a_p}^{1/2} \geq \lim_{r_c \rightarrow \infty} \langle v_\zeta^2 \rangle_{2 a_p}^{1/2} = \left| \frac{dU_\theta}{dt} \right| \frac{\sqrt{12516735}}{5996 B_{\theta c}^2 a_c^2}, \quad (39)$$

and this value is entirely determined by the current-channel radius and the poloidal magnetic field *at the base of the corona*. For efficient energy transport, a significant fraction of the energy transport for flux emergence will occur *in and near* the current channel. The corresponding rms vertical photospheric velocity inside $r \leq 2 a_p$ constrained by the helicity budget is derived in Appendix B

$$\langle v_\zeta^2 \rangle_{2 a_p}^{1/2} = \left| \frac{d\Phi_\theta}{dt} \right| \frac{\sqrt{12516735} |B_{\zeta p}| r_c^2}{8 B_{\theta c} a_c |2998 B_{\zeta p} r_c^2 - 1155 B_{\zeta c} a_c^2|}. \quad [\text{B9}]$$

For comparison, minimizing $\int dr r (\partial_r v_\zeta)^2$ with $v_\theta = 0$ produces the minimum shear estimate (constant velocity $r < r_c$) which has rms vertical photospheric (everywhere) of

$$\langle v_\zeta^2 \rangle_p^{1/2} = \left| \frac{dU_\theta}{dt} \right| \frac{1}{B_{\theta c}^2 a_c^2} \frac{120}{73 + 120 \log(B_{\zeta p} r_c / B_{\zeta c} a_c)}, \quad (40a)$$

for the energy constraint and

$$\langle v_\zeta^2 \rangle_p^{1/2} = \left| \frac{d\Phi_\theta}{dt} \right| \frac{1}{B_{\theta c} a_c} \frac{30}{73 + 120 \log(B_{\zeta p} r_c / B_{\zeta c} a_c)}, \quad (40b)$$

for the helicity constraint.

- Both limits above require wasted flows along field lines $v_\parallel \neq 0$. However by minimizing $\int dr r (v_\theta^2 + v_\zeta^2)$ with $v_\parallel = 0$, the most efficient rms total velocity inside $r \leq 2 a_p$ constrained by the energy budget is derived in Appendix A

$$\langle v^2 \rangle_{2 a_p}^{1/2} = \left| \frac{dU_\theta}{dt} \right| \frac{2 B_{\zeta p} r_c^2 \sqrt{2310} \sqrt{21674 B_{\theta c}^2 + 14421 B_{\zeta c} B_{\zeta p}}}{a_c^2 |B_{\theta c} B_{\zeta p} (23984 B_{\theta c}^2 + 14421 B_{\zeta c} B_{\zeta p}) r_c^2 - 9240 a_c^4 B_{\theta c}^3 B_{\zeta c}|}, \quad [\text{A17a}]$$

and the most efficient rms total velocity inside $r \leq 2 a_p$ constrained by the helicity budget is derived in Appendix B

$$\langle v^2 \rangle_{2 a_p}^{1/2} = \left| \frac{d\Phi_\theta}{dt} \right| \frac{B_{\zeta p} r_c^2 \sqrt{2310} \sqrt{21674 B_{\theta c}^2 + 14421 B_{\zeta c} B_{\zeta p}}}{2 a_c |B_{\zeta p} (23984 B_{\theta c}^2 + 14421 B_{\zeta c} B_{\zeta p}) r_c^2 - 9240 a_c^4 B_{\theta c}^2 B_{\zeta c}|}, \quad [\text{B11}]$$

where $v_\parallel = 0$ everywhere.

These three driving scenarios are used to estimate the expected rms velocities near the current channel of CME flux-rope footpoints.

3.2. Velocity Estimates Constrained by CME Trajectories

The flux-rope model has been fitted to the CME trajectory observed on 2000 September 12 (Chen et al. 2006; Chen & Kunkel 2010). Chen et al. (2006) and Chen & Kunkel (2010) find that the observed dynamics is consistent with a peak poloidal flux injection rate of $d\Phi_\theta/dt = 1.4 \times 10^{19} \text{ Mx s}^{-1}$ and an energy injection of $2 - 4 \times 10^{32} \text{ erg}$ over 40 minutes (James Chen, personal communication 2008 November). The average power requirement of the flux-rope model $\langle dU_\theta/dt \rangle \simeq 1.3 \times 10^{29} \text{ erg s}^{-1}$ is the *lower limit* for the power budget of the CME over 40 minutes—the instantaneous power budget is likely to exceed this value $dU_\theta/dt \geq \langle dU_\theta/dt \rangle$. The separation distance between the filament footpoints and the flux-rope footpoints

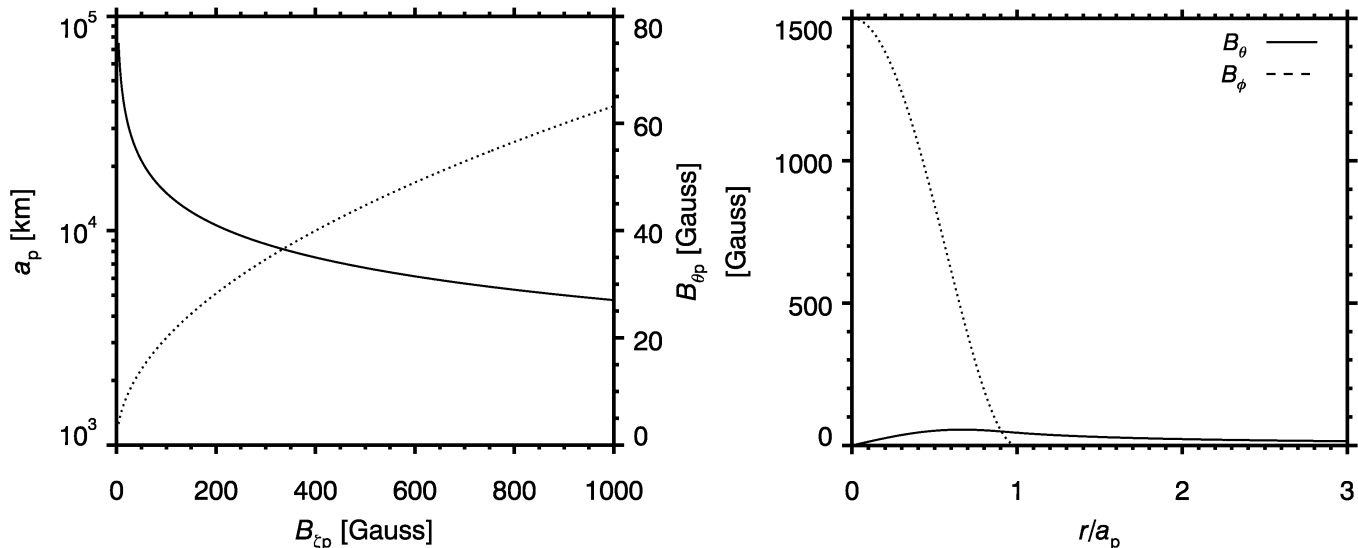


Fig. 3.— left: photospheric current-channel radius a_p (solid line) and poloidal magnetic field $B_{\theta p}$ (dashed line) as a function of the average vertical magnetic field in the current channel $B_{\zeta p}$ assuming coronal parameters consistent with the 2000 September 12 CME trajectory: $a_c = 7.5 \times 10^9$ cm, $B_{\theta c} = B_{\zeta c} \simeq 4$ G. Right: photospheric magnetic field profiles for $B_{\zeta p} = 500$ G

were estimated to be $s_f \simeq 3.5 \times 10^{10}$ cm and $S_f \simeq 5 \times 10^{10}$ cm respectively which leads to a coronal current-channel radius $a_c = (S_f - s_f)/2 \simeq 7.5 \times 10^9$ cm. The magnetic field at the base of the corona is estimated to be $B_{\theta c} = B_{\zeta c} \simeq 4$ G (Chen & Kunkel 2010). Figure 3 shows the photospheric current-channel radius a_p (solid line) and poloidal magnetic field $B_{\theta p}$ (dashed line) as a function of the average vertical magnetic field in the current channel determined from Equations (14a) and (14b).

Figure 4 shows velocity estimates for the 2000 September 12 CME trajectory modeled by Chen et al. (2006) and Chen & Kunkel (2010) as a function of the average vertical magnetic field in the current channel using a cutoff scale $r_c = S_f/2 = 2.5 \times 10^{10}$ cm. The magnitude of the vertical magnetic field can be interpreted as height with $B_{\zeta p} = B_{\zeta c} = 4$ G corresponding to the base of the corona and $B_{\zeta p} \simeq 500$ G corresponding to the photosphere. The solid lines correspond to rms velocities estimated from the energy budget and the dashed lines correspond to rms velocities estimated from the helicity budget. In the left panel, the blue and red lines are the optimal twisting $\langle v_{\theta}^2 \rangle_{a_p}^{1/2}$ and emergence $\langle v_{\zeta}^2 \rangle_{2a_p}^{1/2}$ velocities at the flux-rope footpoint inside $r \leq a_p$ and $r \leq 2a_p$ respectively, corresponding to the minimum velocity solutions in Appendices A and B. The green lines indicate the emergence velocity corresponding to the minimum shear (constant velocity $r < r_c$) solution. In the right panel, the blue, red and black lines correspond to the poloidal $\langle v_{\theta}^2 \rangle_{2a_p}^{1/2}$ and vertical $\langle v_{\zeta}^2 \rangle_{2a_p}^{1/2}$ components of the optimal total velocity $\langle v^2 \rangle_{2a_p}^{1/2}$ respectively with $v_{\parallel} = 0$ at the flux-rope footpoint inside $r \leq 2a_p$. In both panels, the dotted black line is the solar escape velocity $v_{\odot} = 617$ km s $^{-1}$, the dotted green line is the photospheric sound speed $C_s \equiv \sqrt{\gamma p_p / \rho_p} \simeq 7.2$ km s $^{-1}$ with $\gamma = 5/3$, mass density $\rho_p \simeq 5.85 \times 10^{-8}$ g/cm 3 , and pressure $p_p \simeq 1.82 \times 10^{-4}$ g cm $^{-1}$ s $^{-2}$ from VAL-C model for the quiet sun (Vernazza et al. 1981) interpolated to the $\tau = 1$ height of 240 km for Ni I 6767.8 Å line imaged by MDI (Jones 1989; Bruls 1993). The dotted blue line is the average Alfvén speed $\langle V_A \rangle_{2a_p} \equiv \langle B \rangle_{2a_p} / \sqrt{4\pi\rho_p}$ inside $r \leq 2a_p$. The velocities based on the energy and helicity budgets are in close agreement and this

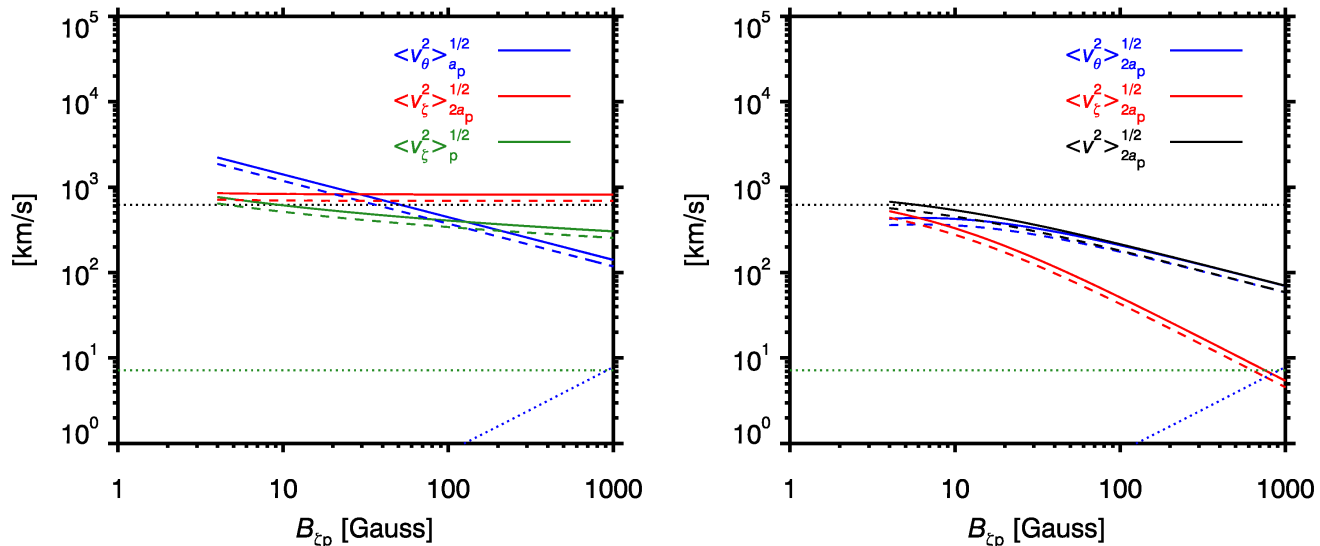


Fig. 4.— Optimal velocity estimates for the 2000 September 12 CME trajectory modeled by Chen et al. (2006) and Chen & Kunkel (2010) as a function of the average vertical magnetic field in the current channel. The solid lines correspond to rms velocities estimated from the energy budget and the dashed lines correspond to rms velocities estimated from the helicity budget. Left: the blue and red lines are the optimal twisting $\langle v_\theta^2 \rangle_{a_p}^{1/2}$ and emergence $\langle v_\zeta^2 \rangle_{2a_p}^{1/2}$ velocities at the flux-rope footpoint inside $r \leq a_p$ and $r \leq 2a_p$ respectively. The green lines indicate the emergence velocities corresponding to the minimum shear (constant velocity, $r < r_c$) solution. Right: the blue, red and black lines correspond to the poloidal $\langle v_\theta^2 \rangle_{2a_p}^{1/2}$ and vertical $\langle v_\zeta^2 \rangle_{2a_p}^{1/2}$ components of the optimal total velocity $\langle v^2 \rangle_{2a_p}^{1/2}$ respectively at the flux-rope footpoint inside $r \leq 2a_p$. (both) The dotted black lines are the solar escape velocity $v_\odot = 617 \text{ km s}^{-1}$, the dotted green lines are the photospheric sound speed $C_s \simeq 7.2 \text{ km s}^{-1}$, and the dotted blue lines are the average Alfvén speed $\langle V_A \rangle_{2a_p}$.

agreement is nontrivial as Equations (37) and (38) indicate. Exact agreement for the magnetic field profile Equations (9a) and (9b) corresponds to

$$\frac{dU_\theta}{dt} = \frac{B_{\theta c} a_c}{4} \frac{d\Phi_\theta}{dt}. \quad (41)$$

Figure 5 shows example optimal velocity and Poynting flux profiles⁷ for the 2000 September 12 CME assuming $B_{\theta c} = B_{\zeta c} \simeq 4 \text{ G}$ and $B_{\zeta p} = 500 \text{ G}$. The dot-dashed lines correspond to the minimum shear (constant velocity $r < r_c$) solution for the vertical velocity. The crossing point between the optimal emergence and constant velocity solutions occurs at the asterisks. The optimal emergence velocity profile v_ζ , constrained by the energy budget, exceeds 1500 km s^{-1} inside the current channel $r \lesssim a_p$ and exceeds 100 km s^{-1} over most of the range $0 < r \lesssim 3a_p$. The Poynting flux should be compared with the radiation emittance at the solar surface $\mathcal{F} \simeq 6.317 \times 10^{10} \text{ erg s}^{-1} \text{ cm}^{-2}$ indicated by the horizontal dotted line in the right panel of Figure 5. All three velocity profiles produce Poynting fluxes which exceed the radiation emittance at the

⁷The optimal solutions for the energy flux and helicity flux are proportional with B_θ in the former replaced with A_θ in the latter and $B_\theta/A_\theta = 2B_{\theta p}/a_p$, $B_{\zeta p} = 2B_{\theta c}/a_c$, $B_{\zeta c} \simeq 2/a_p$. The optimal velocity and helicity flux profiles are proportional to those shown in Figure 5.

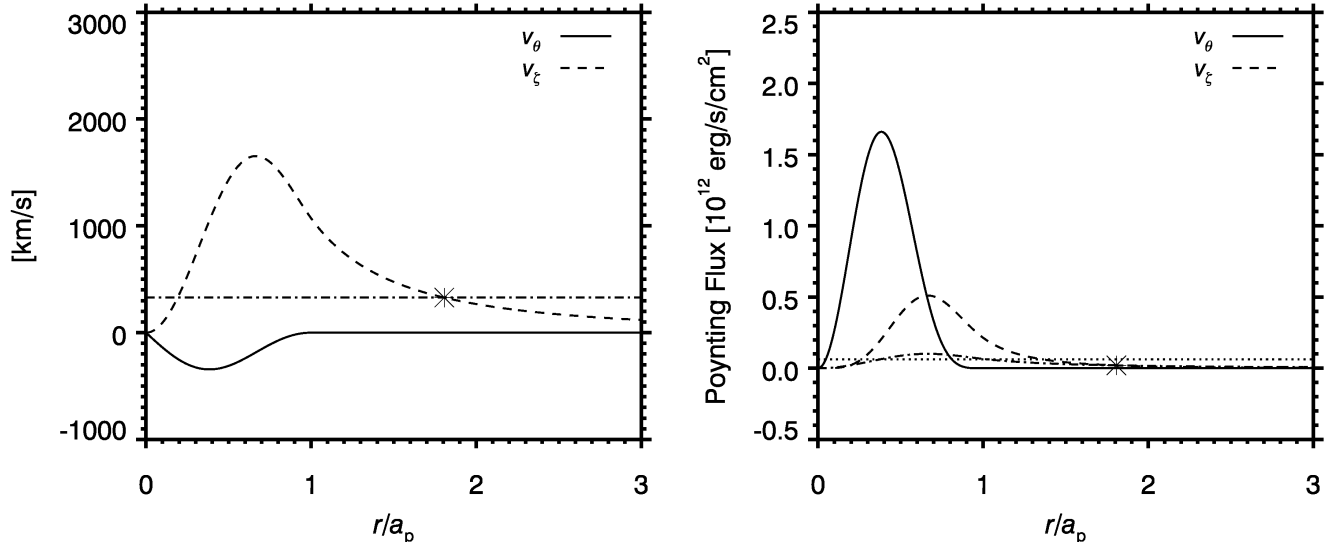


Fig. 5.— Example optimal velocity and Poynting flux profiles in the photosphere for the 2000 September 12 CME assuming $B_{\theta c} = B_{\zeta c} \simeq 4$ G and $B_{\zeta p} = 500$ G. The dot-dashed lines correspond to the minimum shear (constant velocity $r < r_c$) solutions for the vertical velocity. The crossing point between the optimal emergence and constant velocity solutions occurs at the asterisks. The radiation emittance at the solar surface $\mathcal{F} \simeq 6.317 \times 10^{10} \text{ erg s}^{-1} \text{ cm}^{-2}$ is indicated by the horizontal dotted line.

solar surface and the fluxes of white light flare kernels $1 - 2 \times 10^{10} \text{ erg s}^{-1} \text{ cm}^{-2}$ (Neidig 1989). The absence of strong photospheric signatures associated with CMEs suggests that flux injection cannot be responsible for the CME eruption.

3.3. Discussion

I emphasize that the 2000 September 12 event is not an extreme CME. Krall et al. (2006) describe the 2003 October 28 CME, first observed in LASCO C3 images at 11:30 UT, that requires $\Delta U_\theta \simeq 2 \times 10^{33} \text{ erg}$ and $\Delta \Phi_\theta \simeq 6 \times 10^{22} \text{ G cm}^{-2}$ over $\Delta t \simeq 18$ minutes with $a_c = 8.1 \times 10^9 \text{ cm}$, $S_f = 3 \times 10^{10} \text{ cm}$ and $B_{\theta c} = B_{\zeta c} = 3.2 \text{ G}$. The timescale of approximately 15 minutes and energy requirements $2 \times 10^{32} \text{ erg}$ are in close agreement with the estimates used by Manchester et al. (2008) to simulate the initiation and propagation of this eruption. Figure 6 shows optimal velocity estimates for the 2003 October 28 CME/ICME trajectory modeled by Krall et al. (2006) in the same format as Figure 4. This event requires extreme photospheric velocities in the range $v \simeq 2500 - 16000 \text{ km s}^{-1}$ to satisfy the energy budget and $v \simeq 500 - 3000 \text{ km s}^{-1}$ to satisfy the helicity budget.

Returning to the 2000 September 12 event, Figures 4 and 5 indicate that significant photospheric signatures of flux injection should be detectable in or near the current-channel radius $r \lesssim 2 a_p$. For the left panel in Figure 4, corresponding to ideal footpoint twisting *or* flux injection (emergence), all of the rms velocities exceed the local characteristic speeds of an MHD plasma. The optimal rms emergence velocities $\langle v_\zeta^2 \rangle_{2a_p}^{1/2}$ exceed the solar escape velocity $v_\odot = 617 \text{ km s}^{-1}$ inside of $r \lesssim 2 a_p$. Thus, gravitational forces cannot restrain the photospheric material in this region. Even for emergence velocities of 100 km s^{-1} , the

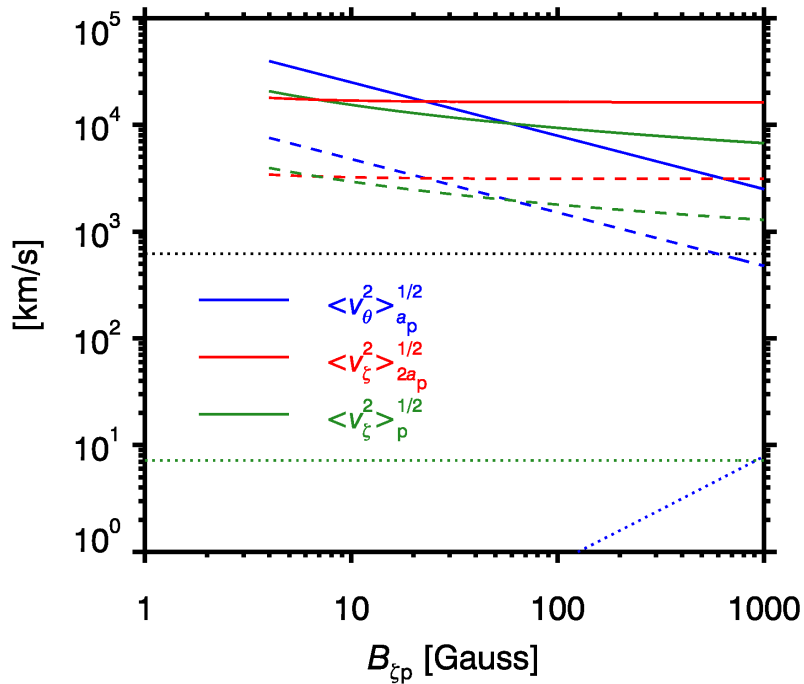


Fig. 6.— Optimal velocity estimates for the 2003 October 28, CME/ICME trajectory modeled by Krall et al. (2006) in the same format as Figure 4.

photospheric material would require 12 minutes to return to the surface by gravity alone and this is roughly the timescale of the 2003 October 28, CME/ICME eruption. Consequently, a characteristic of flux injection should be *hypersonic* upflows concomitant with and preceding the eruption. Optimal photospheric velocities imply a *sustained* mass transport rate of $6 \times 10^{20} \text{ g s}^{-1}$ for just the ring-shaped regions with $v_{\zeta} \geq 617$ maintained over roughly 40 minutes and spatial scales of $\pi a_c^2 \simeq 2 \times 10^{20} \text{ cm}^2$ in the corona (see Figure 9 for the scale of the twice the current channel in the corona). These photospheric flows would eject a net mass of 10^{24} g of which is 9 orders of magnitude larger than the typical CME mass 10^{15} g as estimated from LASCO images. Ballistic photospheric mass outflows of this magnitude should be straight-forward to detect using EIT and LASCO C1 and C2 coronagraphs—mass outflows of this magnitude are not observed by these instruments. It is worth repeating that the rms optimal emergence velocities in the photosphere are largely independent of $B_{\zeta a_p}$ and the cutoff scale r_c and $\langle v_{\zeta} \rangle_{2a_p}^{1/2}$ is asymptotically determined by the values at the base of the corona $B_{\zeta a_c}$ and a_c . The left panel of Figure 4 appears to indicate that the minimum shear velocity (green) is more efficient than either footpoint twisting (blue) or flux injection (red) since it exhibits lower velocities inside $r \leq 2a_p$. However the left panel of Figure 5 shows that this is simply because the profiles of the optimal twisting and emergence velocities reduce to essentially zero beyond $r = a_p$ and $r \gtrsim 1.75a_p$ respectively whereas the minimum shear velocity remains constant out to the cutoff scale r_c . For the right panel in Figure 4, corresponding to combined footpoint twisting *and* flux injection (emergence), flux emergence is only efficient when $B_{\theta} \simeq B_{\zeta}$. For $B_{\zeta} \gg B_{\theta}$ footpoint twisting is more efficient for transferring energy and helicity from the photosphere to the corona.

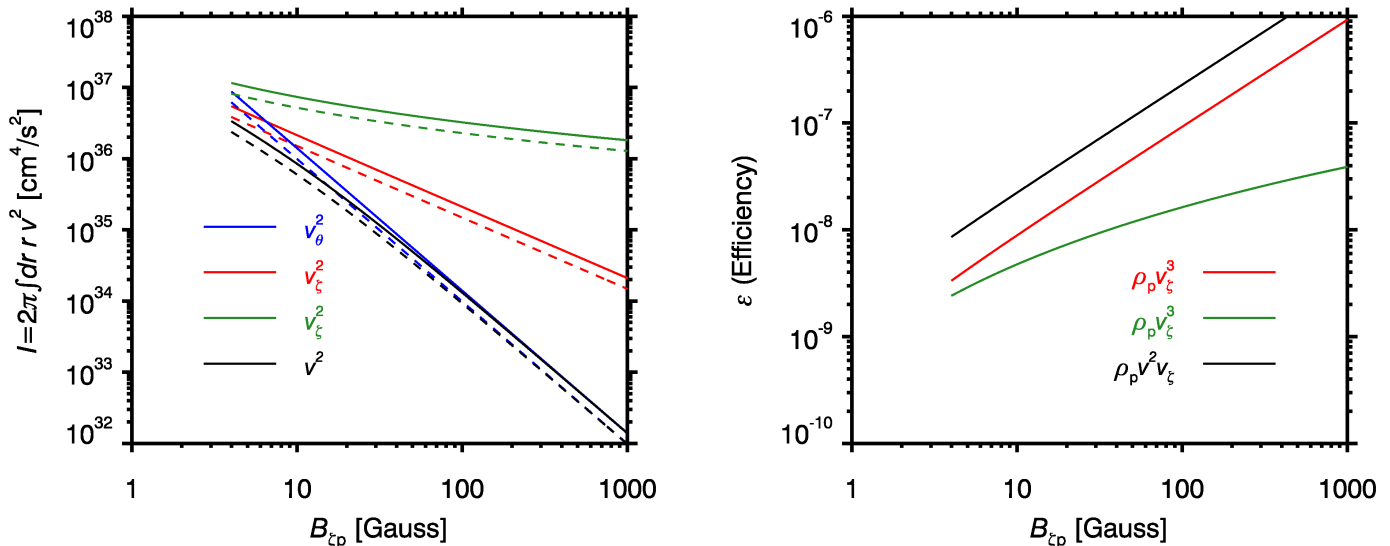


Fig. 7.— Efficiencies of the driving scenarios for the 2000 September 12 CME. Left: density normalized kinetic energy $I = \mathcal{I}/\rho_p$ in a horizontal slice and right: ratio of the kinetic energy transport across the photosphere to the magnetic power requirements of the CME under the flux-injection hypothesis. The solid lines correspond to rms velocities estimated from the energy budget and the dashed lines correspond to rms velocities estimated from the helicity budget. Blue, red, green, and black lines correspond to optimal twisting, optimal emergence, minimum shear (constant velocity $r < r_c$), and optimal combined twisting and emergence velocity profiles respectively (blue line is not shown in right panel).

The efficiencies of the processes may be ranked either with the magnitude of the integral

$$\mathcal{I} = 2 \pi \rho_p \int_0^{r_c} dr r v^2, \quad (42a)$$

or

$$\epsilon \equiv \frac{|dU_\theta/dt|}{|dU_\theta/dt| + 2 \pi \rho_p \int_0^{r_c} dr r v^2 v_\zeta}, \quad (42b)$$

where $F = \pi \rho_p \int_0^{r_c} dr r v^2 v_\zeta$ is the kinetic energy flux through the photosphere integrated over one foot-points. The former metric is simply the photospheric kinetic energy which is used to optimize the velocity profiles, whereas the latter metric is the ratio of the power requirements of the CME to the total energy transported across the photosphere under the flux-injection hypothesis.

Figure 7 shows the efficiencies of the driving scenarios for the 2000 September 12 CME based on \mathcal{I} , the kinetic energy in a horizontal slice (Equation (42a)) and ϵ , the ratio of the magnetic power requirements of the CME to the total energy transported across the photosphere (Equation 42b) under the flux-injection hypothesis in the left and right panels respectively. The solid lines correspond to rms velocities estimated from the energy budget and the dashed lines correspond to rms velocities estimated from the helicity budget. Blue, red, green, and black lines correspond to optimal twisting, optimal emergence, minimum shear, and optimal combined twisting and emergence velocities respectively—the blue line is not shown in the right panel because the efficiency is $\epsilon = 1$. Based on either criterion (42a) or (42b) the minimum shear (constant velocity $r < r_c$) is the *least* efficient velocity profile (shown in green) for transporting magnetic energy across the photosphere on the timescale of the eruption. However, the most efficient velocity is different for \mathcal{I} and ϵ .

Using the photospheric kinetic energy \mathcal{I} , the combined twisting and emergence is the most efficient velocity profile (shown as the black line in the left panel). Using the ratio of the magnetic power requirements of the CME to the total energy transported across the photosphere ϵ , footpoint twisting is the most efficient velocity profile ($\epsilon = 1$) because footpoint twisting does not transport mass across the photosphere—the velocity field is tangent to the surface.

The left panel Figure 7 shows that, for small vertical magnetic fields $B_{\zeta p} \lesssim 10$ G, the kinetic energy \mathcal{I} for pure emergence is slightly less than for pure footpoint twisting. For $B_{\zeta p} \gtrsim 10$ G, the kinetic energy for footpoint twisting less than for pure emergence. Consequently, the twisting motions dominate the kinetic energy of the combined twisting and emergence velocity profile since twisting motions are more efficient for transporting energy and helicity into the corona. The combined twisting and emergence velocity profile might be more efficient than the right panel of Figure 7 indicates. The rms vertical velocities for this solution in Figure 4 do not exceed the escape velocity and significant photospheric material could *eventually* return to the surface via strong downflows along magnetic fields.

4. COMPARISON AGAINST PHOTOSPHERIC OBSERVATIONS

The vertical photospheric plasma velocities in and near the current channel of the CME footpoints must be large to satisfy the flux-injection hypothesis. Such extreme velocities probably would have been detected in previous studies of CME eruptions, but not no such observations have been reported in the literature. Nonetheless, comparing expected values with observations is a necessary final step to establish the likelihood that a theory is compatible with nature. High spatial resolution high-cadence (~ 1 minute) line profiles would be ideal for examining the footpoints of CMEs during eruptions. This suggests that limited field-of-view line-profile data would be the best candidate data set (see Harra et al. 2007; Imada et al. 2007, for observations of coronal outflows during the gradual phase of a flare). However, CME footpoints are always identified post-facto and are usually outside the main flux concentration of the active region that is often the focus of high-resolution campaigns. Thus, full-disk data are required to ensure that the dynamics of both CME footpoints are captured. Full-disk line-profile data are presently scarce. One possible candidate is the Naval Research Laboratory *Skylab* He II 304 Å spectroheliograms with $2''$ spatial resolution, but these observations are usually at low temporal cadence relative to flare/CME dynamics, in the wrong wavelength range for photospheric observations, and are difficult to disambiguate—the spatial and wavelength information is convolved. Finally, for direct comparison with the flux-rope model, photospheric observations concomitant with published results are desirable (Chen et al. 1997, 2000; Wood et al. 1999; Krall et al. 2001; Chen et al. 2006; Krall et al. 2006; Chen & Kunkel 2010)—and this event must correspond to a front-side CME to ensure that both footpoints are visible in the photosphere.

After surveying the CMEs modeled with the flux-rope model, the 2000 September 12 CME (Chen et al. 2006; Chen & Kunkel 2010) was determined to be the best candidate because: (1) the event was front side and associated with a M1.0 flare, (2) the filament footpoint locations identified in (Chen et al. 2006) were distinct from the flare ribbons simplifying the interpretation of the observed emission lines, and (3) the dynamics of the filament was captured by EIT, LASCO C2 and C3 coronagraphs, and KSO $H\alpha$ -observations. The MDI instrument was in Flarewatch mode on this day, but there is a gap in high-cadence coverage during the flare between 07:00 UT and 15:30 UT. However, the solar oscillations investigation (SOI) aboard *SOHO* provides continuous monitoring of Doppler velocities of low- to intermediate degree l (Scherrer et al. 1995). The medium- l data are the result of Gaussian spatial filtering to mitigate spatial aliasing followed by a reduction in resolution from 1024×1024 pixels at $2''$ pixel $^{-1}$ to 192×192 at roughly $10''$ pixel $^{-1}$. This is

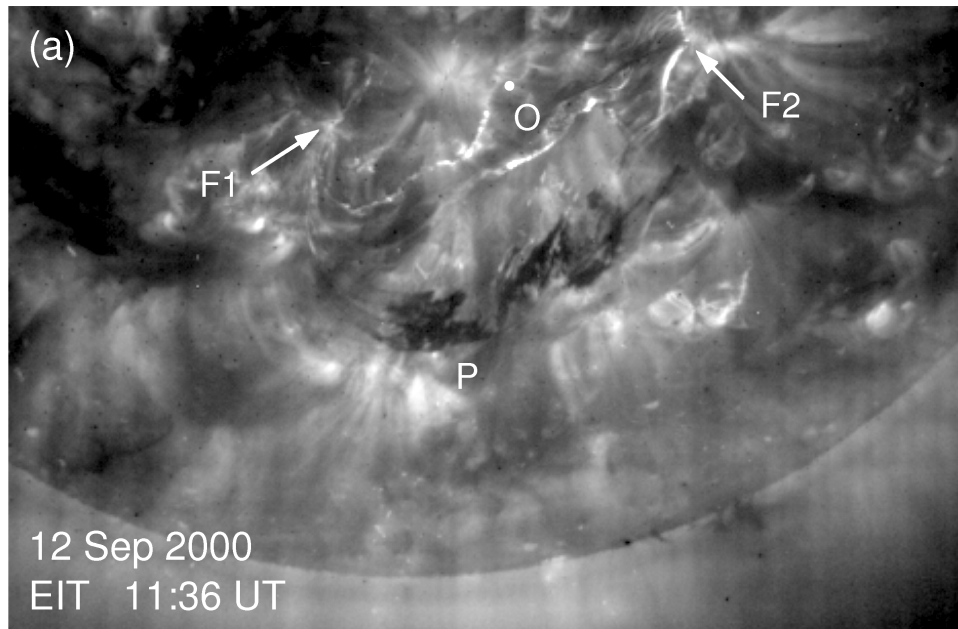


Fig. 8.— Source region of eruption observed by EIT (Fe XII 195 Å) at 11:35 UT. The erupting prominence, denoted by “P” appears as a dark absorption feature. The prominence footpoints are indicated “F1” and “F2” and their midpoint is designated “O.” The time 11:36 in the figure indicates the *uncorrected start time*. After Figure 2(a) in Chen et al. (2006).

supplemented with level 1.8.2 2'' 5-minute averaged 96-minute cadence magnetograms with the most recent magnetic field inter-calibrations (Tran et al. 2005; Ulrich et al. 2009).

Chen et al. (2006) identified the locations F1 and F2 of the prominence footpoints in the EIT (Fe XII 195 Å) image shown in Figure 8. Using these locations, the nominal geometry of the flux-rope model for the base of the corona and photosphere is diagrammed in Figure 9. The top shows the EIT (Fe XII 195 Å) image at 11:35 UT and the bottom shows the MDI (Ni I 6767.8 Å) at 11:15 UT differentially de-rotated to 11:35 UT to match the time of the EIT image using Dominic Zarro’s mapping package.⁸ The filament and nominal current-channel footpoints are distinct from the flare ribbons in the EIT image. The dark curved adsorbtion feature in the EIT image spanning $-175''$ to $400''$ in X and $-375''$ to $-675''$ in Y is the filament.

The MDI level 1.8.2 magnetograms (BLDVER18=60100) incorporate the latest sensitivities from inter-calibrations with the Mount Wilson Observatory (Tran et al. 2005; Ulrich et al. 2009). The line-of sight magnetic field was corrected for geometrical effects with a factor of μ^{-1} assuming that the field is purely vertical where

$$\mu = \frac{R_{\odot} - D_{\odot} \sqrt{1 - \varrho_1^2/R_{\odot}^2}}{\sqrt{R_{\odot}^2 - 2 R_{\odot} D_{\odot} \sqrt{1 - \varrho_1^2/R_{\odot}^2} + D_{\odot}^2}} \approx \sqrt{1 - \varrho_1^2/R_{\odot}^2}, \quad (43)$$

where the impact parameter ϱ_1 (radians) is measured from disk center, R_{\odot} is the radius of the Sun in the telescope (radians or arcsecs), and R_{\odot}/D_{\odot} is the ratio of the radius of the Sun to the distance between the

⁸The SolarSoft mapping software is located at <http://www.lmsal.com/solarsoft/gen/idl/maps/>.

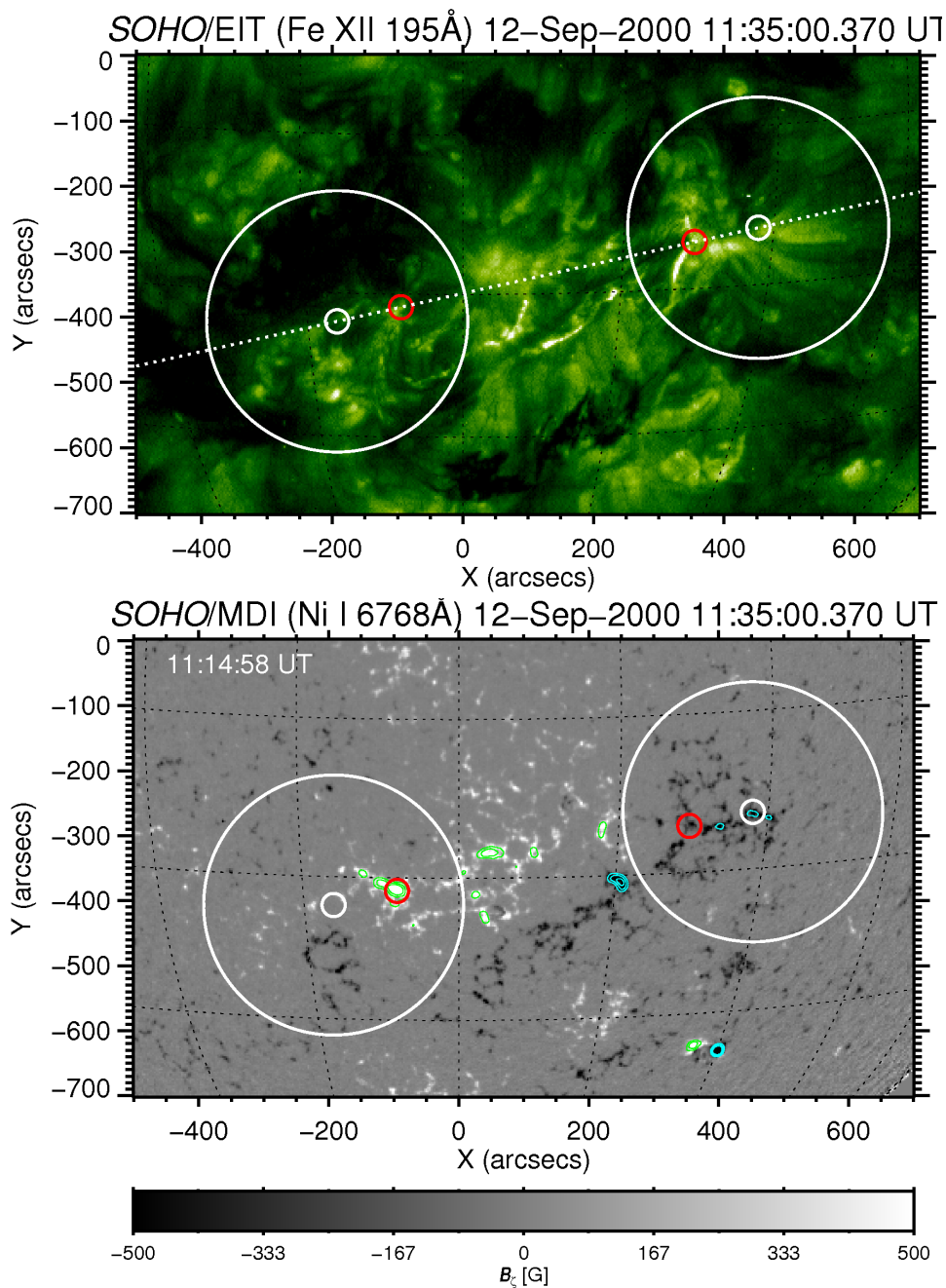


Fig. 9.— Nominal geometry of the flux-rope model for the base of the corona and photosphere. Top: EIT (Fe XII 195 Å) at 11:35 UT. Bottom: MDI (Ni I 6767.8 Å) at 11:15 UT de-rotated to 11:35 UT to match the time of the EIT image. The red circles correspond to the filament footpoints in Figure 8. The small and large white circles correspond to the extent of twice the current-channel radius in the photosphere and corona respectively assuming $B_{\zeta_p} \simeq 500$ G and $B_{\zeta_c} \simeq 4$ G. Cyan and green contours correspond to average magnetic fields of $(-500, -400, -300)$ and $(300, 400, 500)$ GE respectively on a scale size of 1.5×10^{18} cm².

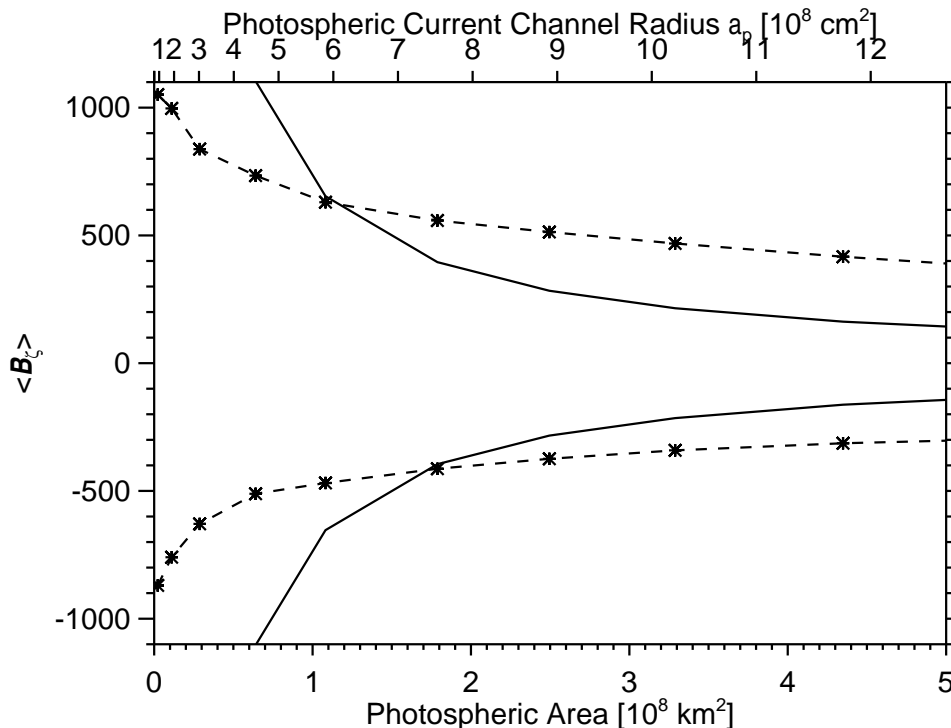


Fig. 10.— Estimate for the vertical magnetic field (flux-rope toroidal magnetic field) in the photosphere. Asterisks connected by dashed lines are the largest magnitude MDI values adjusted for line-of-sight projection and averaged over circular masks with increasing areas within the large white circles of Figure 9. Solid lines are $B_{\zeta P} = B_{\phi c} a_c^2 / a_p^2$ estimated from the flux-rope model with $B_{\phi c} = 4$ G and $a_c = 7.5 \times 10^9$ cm. The top and bottom lines correspond to the left and right footpoints of the flux rope. See the text for discussion.

observer and Sun center. Chen et al. (2006) argue that the filament footpoints shown in red and the nominal current-channel footpoints are not co-located, but are related by

$$S_f = s_f + 2 a_c. \quad (44)$$

This idealized geometry is reflected in Figure 9 where the red circles correspond to the filament footpoints in Figure 8 and the large and small white circles correspond to the extent of twice the current-channel radius in the corona and photosphere respectively. The left large white circle is associated with mainly positive magnetic field and the right large white circle is associated with mainly negative magnetic field.

The current-channel radius in the photosphere should be determined by enforcing consistency between the flux-rope model photospheric extrapolation and the MDI magnetogram through flux conservation (Equation (10a)). The current-channel radius at the base of the corona is $B_{\zeta c} \simeq 4$ G with a radius $a_c = 7.5 \times 10^9$ cm (Chen et al. 2006). If all the toroidal flux in the coronal current channel mapped to a single MDI pixel at disk center the resulting magnetic field would exceed 30 kG. Such extreme values of magnetic field have never been observed in the photosphere. Consequently, the photospheric current channel will be larger than one MDI pixel except perhaps very near the limb. To estimate the current-channel size in the photosphere while minimizing discrepancies between the photospheric observations and the flux-rope model, circular masks of increasing scale size were computed. These masks were convolved with the MDI values adjusted for line-

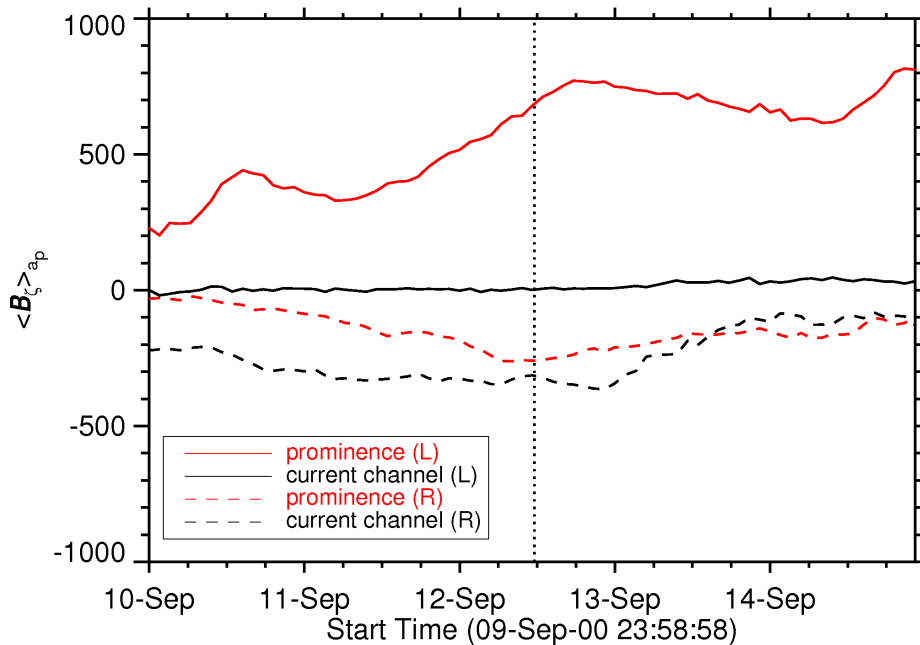


Fig. 11.— Temporal development of the average vertical magnetic field within $r \leq a_p \simeq 6.7 \times 10^8$ cm for the left (L) and right (R) filament and current-channel footpoints shown in Figure 9. The vertical dashed line corresponds to the rise of the M-class flare.

of-sight projection in regions bounded by both the left and right large white circles in Figure 9. At each scale, the maximum magnitude magnetic fields were selected from the output of the convolution and plotted as asterisks connected by dashed lines in Figure 10; these values correspond to the maximum magnitude average magnetic field at that scale size contained within the regions bounded by the large white circles in Figure 9. The solid lines are $B_{\zeta p} = B_{\phi c} a_c^2 / a_p^2$ estimated from the flux-rope model with $B_{\phi c} = 4$ G and $a_c = 7.5 \times 10^9$ cm. The top and bottom lines correspond to the left and right footpoints of the flux rope. The photospheric extrapolation of flux-rope model agrees with the MDI magnetogram where the solid and dashed lines cross. The photospheric area most consistent with the constraints of the flux-rope model is $1 - 2 \times 10^8$ km² corresponding to a current-channel radius of $a_p \simeq 6.7 \times 10^8$ cm and an average photospheric toroidal field of $\langle B_{\zeta p} \rangle \simeq 500$ G.

The geometrical relationship (44) proposed in Chen et al. (2006) isn't entirely consistent with the photospheric observations in Figure 9. For the left footpoint, the main concentration of positive flux is associated with the filament footpoint not the nominal current channel. Indeed the magnetic field in the nominal current channel ranges from -24 to +24 G. For the right footpoint the magnetic field pixel ranges in the filament footpoint and the nominal current channel are similar ranging from -665 to -42 G and -600 to -62 G respectively. However, the average magnetic field magnitude in the right nominal filament footpoint does not exceed 300 G whereas the magnitude in the nominal current channel is somewhat higher as indicated by the cyan contour corresponding to -300 G contained within the small white circle. Figure 11 shows the temporal development of the average vertical magnetic field within $r \leq a_p \simeq 6.7 \times 10^8$ cm for the left (L) and right (R) filament and current-channel footpoints shown in Figure 9. The vertical dashed line

corresponds to the rise of the M-class flare. Around the time of the flare, the vertical flux is strengthening at the left prominence footpoint at a rate of $8 \times 10^{15} \text{ Mx s}^{-1}$, but the flux in the nominal left current channel remains near zero over the whole five day period. The average fluxes at the right prominence and current-channel footpoints are flat around the eruption time. The flux-imbalance between the left and right footpoint indicates that the connectivity between these photospheric magnetic features is not trivial.

While gravity certainly effects the height of the heavy prominence material potentially producing a difference between the position of the prominence material and the center of the current channel at the apex of the flux rope, there is no stated reason in Chen et al. (2006) for why the flux-rope current-channel and prominence footpoints aren't co-located in the photosphere.⁹ The footpoint separation S_f is a critical parameter because the height H_{max} of the maximum acceleration for the CME scales with S_f in the flux-rope model $S_f/2 \leq H_{\text{max}} \lesssim 3/2 S_f$ (Chen et al. 2006; Chen 2007). If S_f is not consistent with observations, then the flux-rope model cannot be correct.

4.1. Doppler Data Preparation

The MDI vector-weighted Dopplergrams were analyzed following the procedures outlined in Snodgrass (1984) and Hathaway (1992). First, the motion of the observer was removed from each Dopplergram using

$$V_{SOHO}(\varrho_1, \psi) = V_R (1 - \varrho_1^2/2) + V_W \varrho_1 \sin \psi - V_N \varrho_1 \cos \psi, \quad (45)$$

where the impact parameter ϱ_1 (radians) is measured from disk center and the position angle ψ (radians) measured counterclockwise from solar north are the heliocentric radial coordinates and V_R , V_W , and V_N are the *SOHO* satellite velocities radial outward, westward parallel to equator, and northward along the rotation axis, respectively, using the appropriate keywords provided with the MDI data.

Second, the Dopplergrams are co-registered and time-averaged. The time-averaged Dopplergram was fitted with orthonormal disk functions to eliminate cross-talk between coefficients (Snodgrass 1984).

$$\bar{V}(B_0, \varrho, \Theta, \Phi) = \omega(\Theta) R_\odot \sin \Phi \cos B_0 + V_{\text{LS}}(\varrho) + V_{\text{MF}}(\Theta) + H \sin \Theta, \quad (46a)$$

where differential rotation profile

$$\omega(\Theta) = \sum_{n=0}^2 A_{2n} T_{2n}^1(\sin \Theta) \quad (46b)$$

is expanded in a truncated series of even orthonormal Gegenbauer polynomials (Morse 1953), the limbshift function is represented by

$$V_{\text{LS}}(\varrho) = \sum_{n=0}^4 L_n \mathcal{L}_n(1 - \cos \varrho), \quad (46c)$$

with (see pp. 174-175 in Smart 1977)

$$\varrho = -\varrho_1 + \arcsin [D_\odot \sin(\varrho_1) / R_\odot], \quad (46d)$$

⁹Although, the radius of the current channel at the footpoint is defined at the base of the corona the footpoints separation is fixed by the “dense subphotospheric plasma” (see pp. 457 in Chen 1989) or the “massive photospheric density” (Chen & Garren 1993, see pp. 2320) (see also Krall et al. 2000; Chen et al. 2008). This implies that S_f and s_f should be interpreted as photospheric footpoint separations (see also Chen & Krall 2004).

and the meridional flow represented by

$$V_{\text{MF}}(\Theta) = \sum_{n=1}^2 M_n \mathcal{M}_n(\sin \Theta) S(\Theta) (\cos \Phi \sin \Theta \cos B_0 - \cos \Phi \sin B_0), \quad (46e)$$

are expanded in truncated series of $(1 - \cos \varrho)$ and Fourier series of latitude respectively where the function classes $\mathcal{L}_n(x)$ and $\mathcal{M}_n(x)$ were orthonormalized by the Gram-Schmidt procedure on the interval $(0, 1)$ by Snodgrass (1984). The latitude, longitude, and solar-B angle are denoted Θ , Φ and B_0 respectively and $\varrho = \arcsin(\varrho_1/R_\odot)$ is the angle measured from the center of the Sun between the sub-Earth point and a point on the surface of the Sun and $S(\Theta) = +1$ for $\Theta > 0$ and $S(\Theta) = -1$ for $\Theta < 0$.

The function (46a) was fitted to the time-averaged Dopplergram with the standard deviations estimated from the variance of each pixel from its respective time average. The results, with a weighted $\chi^2 = 3898.0$ and 25455 degrees of freedom, are summarized in Table 1. The first four rows of entries represent the best estimate of each parameter $\hat{\theta}$, their standard deviations $\hat{\sigma}$, their t -scores $\hat{t} \equiv \hat{\theta}/\hat{\sigma}$, and their two-sided significance probability in percent that the coefficients would be larger by chance—the smaller the probabilities, the more significant the coefficients. The fifth and sixth rows represent the average parameter estimates $\hat{\mu}$ and population standard deviations $\hat{\sigma}_\mu$ from Table 2 in Snodgrass (1984) for the data taken between 1967 January 1 and 1984 March 5 at the Mount Wilson Solar Observatory (WSO). The seventh and eighth rows represent the t -scores $\hat{t}_{\theta\mu} = (\hat{\theta} - \hat{\mu}) / \sqrt{\hat{\sigma}_\theta^2 + \hat{\sigma}_\mu^2}$ and their two-sided significance probability in percent that the best estimates $\hat{\theta}$ and the population averages $\hat{\mu}$ would differ more by chance—the larger the probabilities, the better the two results agree. All of the best estimates are within one rms standard deviation of the population averages reported by Snodgrass (1984).

The best estimates were used to construct a model line-of-sight velocity for the solar disk which was subtracted from each co-registered Dopplergram and then the Dopplergrams were de-rotated to coincide with the time of EIT image in Figure 9 to produce the residual velocity Δv_{LOS} . The time average of the residual Doppler images is shown on the top left of Figure 12. The red circles correspond to the filament footpoints and the large and small white circles correspond to the extent of twice the current-channel radius in the corona and photosphere respectively.

Unfortunately the MDI Dopplergrams are not absolutely calibrated. The limb-shift coefficient $L_0 = 131 \pm 19 \text{ m s}^{-1}$ represents a constant offset for the Dopplergram series. Since the coefficient is in excellent agreement with measurements by (Snodgrass 1984), cross-calibration against WSO with a laboratory source could permit absolute calibration of MDI Doppler velocities. The well known pseudo redshift in active regions contributes the ambiguity. The top right panel of Figure 12 shows a two-dimensional histogram pairing the magnitude of the magnetic field and the Doppler velocity. The magnetic data were computed by spatially filtering the 96-minute MDI magnetograms (also de-rotated to coincide with the time of the EIT image) with a two-dimensional Gaussian kernel consistent with the Medium- l program ($a = 4$ in Kosovichev et al. 1996) followed by subsampling to the resolution of the Medium- l program. Each Dopplergram was compared to the magnetogram that minimized differences in observation times. This panel demonstrates that the Doppler velocities in magnetic regions are systematically redshifted with respect to the quiet sun with $B = 0$. The histogram with $|B| < 1 \text{ G}$ is Gaussian with an offset of $-2.6 \pm 0.2 \text{ m s}^{-1}$ and a standard deviation of $\sigma = 65.7 \pm 0.1 \text{ m s}^{-1}$. Fitting a fifth degree polynomial to the scatterplot of $\langle \Delta v_{\text{LOS}} \rangle$ versus B produces the line in the right panel described by

$$\langle v_{\text{LOS}} \rangle(B) = \sum_{n=0}^5 q_n B^n, \quad (47a)$$

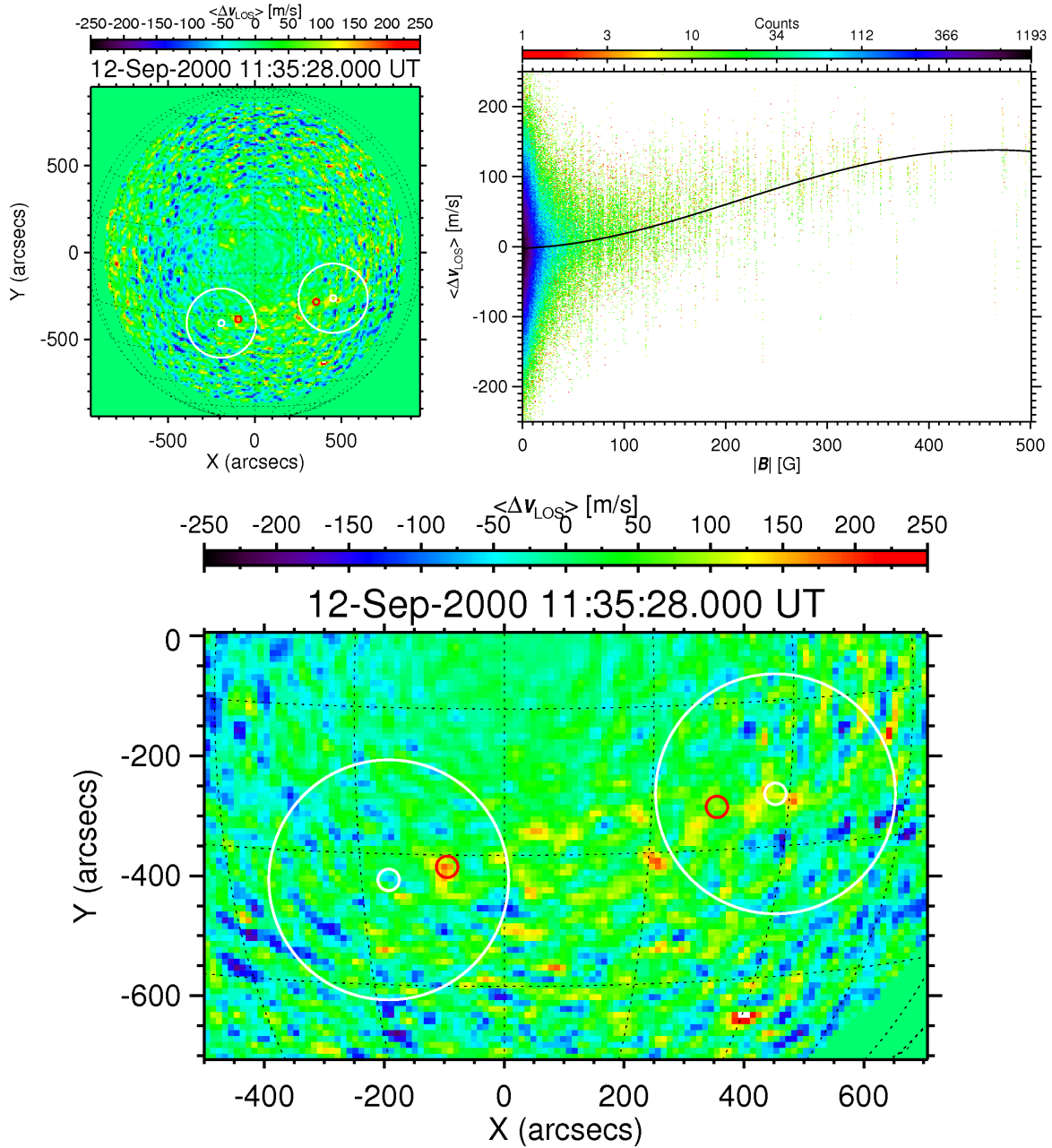


Fig. 12.— Top left: residual full disk Doppler velocities from the Medium- l program averaged over 24 hr. Top right: histogram showing the correlation between the magnitude of the magnetic field and the time-averaged residual Doppler velocity. Bottom: magnified view of the time-averaged residual Doppler velocities in the region containing the filament. The red circles correspond to the filament footpoints and the large and small white circles correspond to the extent of twice the current-channel radius in the corona and photosphere, respectively.

where

$$q_0 = -2.2 \pm 0.1 \text{ m s}^{-1}, \quad (47b)$$

$$q_1 = (5.3 \pm 0.4) \times 10^{-2} \text{ m s}^{-1} \text{ G}, \quad (47c)$$

$$q_2 = (1.75 \pm 0.02) \times 10^{-3} \text{ m s}^{-1} \text{ G}^{-2}, \quad (47d)$$

$$q_3 = (-1.56 \pm 0.08) \times 10^{-6} \text{ m s}^{-1} \text{ G}^{-3}, \quad (47e)$$

$$q_4 = (-4.53 \pm 0.09) \times 10^{-9} \text{ m s}^{-1} \text{ G}^{-4}, \quad (47f)$$

$$q_5 = (4.9 \pm 0.2) \times 10^{-12} \text{ m s}^{-1} \text{ G}^{-5}. \quad (47g)$$

However, this apparent pseudo redshift in magnetic regions is actually produced by the blueshifting of the quiet-sun regions caused by convective motion and the brightness velocity correlation in the convection cells.¹⁰ The convective blueshift is suppressed in magnetic regions causing them to appear redshifted relative to the quiet sun. Consequently, the Doppler shifts may only be discussed relative to the quiet-sun motions which dominate the coefficient L_0 and serve as the zero-point Doppler velocity of Δv_{LOS} .

Third, the p -mode oscillations are removed from the residuals by temporal filtering. Hathaway et al. (2000) employ a Gaussian weighted average of 31 Dopplergrams to reduced the p -mode signal in the 2–4 mHz frequency band where the weights are given by

$$W_i = \frac{w_i}{\sum_{i=-15}^{15} w_i}, \quad (48a)$$

with

$$w_i = \exp\left(-\frac{\Delta t_i}{2\alpha^2}\right) - \exp\left(-\frac{\beta^2}{2\alpha^2}\right) \left(1 + \frac{\beta^2 - \Delta t_i^2}{2\alpha^2}\right) \quad (48b)$$

and $\Delta t_i \equiv t_i - t_0$ is the time difference of the central Dopplergram with $\alpha = 8$ minutes and $\beta = 16$ minutes.

Alternatively, nonparametric uniform B-splines $\hat{h}_m(\boldsymbol{\eta}|t) = \sum_{k=1}^N \eta_k B_{k,2m-1}(t)$ may be employed to filter temporally the data. B-splines are solutions to the optimization problem

$$\min \left[\sum_{i=1}^N \frac{[\hat{h}_m(\boldsymbol{\eta}|t_i) - v_i]^2}{\delta v_i^2} + \lambda \int_{-\infty}^{\infty} dt \left[\frac{d^m \hat{h}_m(\boldsymbol{\eta}|t)}{dt^m} \right]^2 \right], \quad (49)$$

where the summation is the weighted $\hat{\chi}_m^2$, δv_i^2 are the uncertainties, N is number of data or knots, m is the spline half-order, and $\boldsymbol{\eta} \equiv \boldsymbol{\eta}(\lambda)$ is a vector of B-spline parameters and a function of the global regularization parameter $\lambda \geq 0$ (Woltring 1986). The variational principle (49) may be justified by Bayesian arguments when the data v_i is associated with certain priors (see Craven & Wahba 1979, and references therein). The parameter λ controls the balance between smoothness measured by the m th derivative and fidelity measured by the variance with $\lambda \rightarrow 0$ corresponding to spline interpolation with $\hat{\chi}_m^2 = 0$ and $\lambda \rightarrow \infty$ corresponding to a least squares polynomial of order $P_m = m$, degree $d = m - 1$. The boundary conditions at $t = t_1$ and t_N are determined by $d^m \hat{h}_m/dt^m = 0$, where $m = 1, 2, \dots$, consistent with a well-posed solution to the variational principle.

B-spline basis functions have many attractive properties for filtering. For example, they do not require uniform sampling, they adapt to local structure, and the effect of outliers is localized because the basis

¹⁰P. Scherrer and B. Welsch, personal communication 2009 September; see also Dravins (1982) and Bumba & Klvaňa (1995).

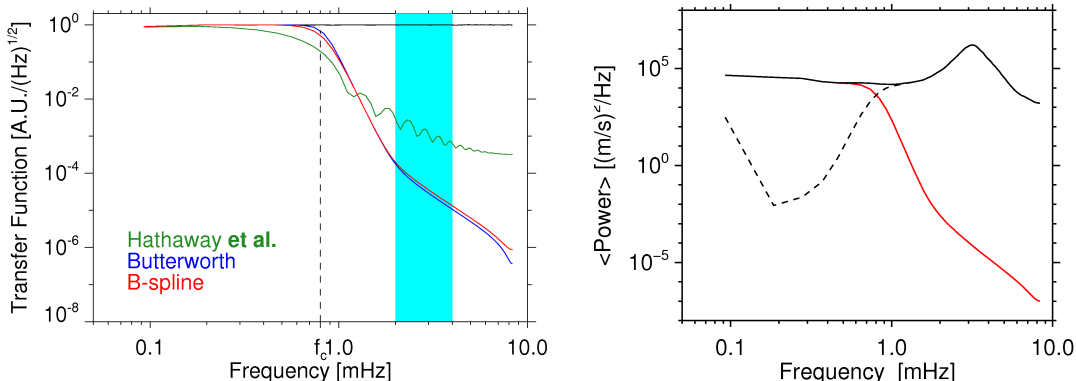


Fig. 13.— Left: the white noise filter responses for the Gaussian weighted average filter from Hathaway et al. (2000) in green, and two $m = 5$ th order cascaded Butterworth filter with $f_c = 8$ mHz in blue and the B-spline filter in green. The filter responses were constructed with 500 realizations of a 24 hr white noise time series with $\Delta t = 1$ minute whose average spectrum is shown in black. The 2–4 mHz regime is shaded in light blue. Right: average power spectra of co-registered and de-rotated Doppler time-series from the inner 10% of the solar disk where the solid black line denotes the unfiltered data exhibiting an enhanced p -mode spectrum in the 2-5 mHz, the solid red line is for the smoothed results after B-spline filtering, and the dashed black line is for the residual data (unfiltered minus smoothed). Both left and right: the spectra were computed using 3 hr segments with 50% overlap.

functions are defined on compact support. For the special case of uniformly sampled, uniformly weighted, periodic data, the spline smoother behaves as two cascaded m th order Butterworth filters without phase distortion; thus B-splines may be viewed as a generalized low pass filter adapted for *nonuniform weighting*, *uneven sampling*, and *non-periodic boundary conditions* (Craven & Wahba 1979). Butterworth filters are an approximation to an ideal filter because they have maximally flat frequency response in the passband and are monotonically decreasing roll-off in the stop-band (Butterworth 1930).

The left panel of Figure 13 shows the filter responses for the Gaussian weighted average filter from Hathaway et al. (2000) in green, and the two $m = 5$ order cascaded Butterworth filters with $f_c = 8$ mHz in blue and the B-spline filter in red with $\tau = 1/f_c = 1250$ s and

$$\lambda = \left[\left(\frac{\tau_c}{2\pi} \right)^{2m} - \left(\frac{2\Delta t}{2\pi} \right)^{2m} \right] / \Delta t = 1.62 \times 10^{21} \text{ s}^9. \quad (50)$$

The filter responses were constructed with 500 realizations of a 24 hour white noise time series with $\Delta t = 1$ minute whose average spectrum is shown in black. The 2–4 mHz regime is shaded in light-blue. The B-splines exhibit a flatter power spectrum in the pass-band and a steeper roll-off in the stop-band than the Gaussian filter. Furthermore, the B-spline filter does not exhibit any ripples in the stop-band. Finally, the B-spline filter can accommodate occasional missing data or uneven sampling and simultaneously interpolate to a different temporal grid as part of the filtering process. Indeed, the B-spline filters were used to replace missing data in the central regions of four MDI Dopplergrams. The right panel of Figure 13 shows the average power spectra of co-registered and de-rotated Doppler time series from the inner 10% of the solar disk where the solid black line denotes the unfiltered data exhibiting an enhanced p -mode spectrum in the 2-5 mHz, the solid red line is for the smoothed results after B-spline filtering, and the dashed black line is for the residual data (unfiltered minus smoothed). The peak power of the p -mode oscillation at $f \simeq 3.15$ mHz

is reduced by a factor of 10^{-10} .

4.2. Photospheric Doppler Signatures During the CME

Figure 14 shows the line-of-sight velocity (top) and the rms line-of sight velocity (bottom) averaged over the current channel of radius $a_p = 6.7 \times 10^8$ cm for the filament channel (red) and current channels (black) on the left (solid) and right (dashed) side of Figure 9 and the soft X-ray flux observed by GOES 8 (blue). The M-class flare associated with the 2000 September 12 CME occurs shortly after 11:30 UT. As discussed in the previous section, all velocities are measured relative to the quiet sun which serves as the zero-point. The top plot shows that the average velocity in the left and right prominence channel and in the right current channel is redshifted with respect to the quiet sun. The left current channel show some evidence of some blueshift (upflows) with respect to the zero-point in the range of -60 to $+10$ ms^{-1} . These velocities are within the standard deviation of $\sigma = 65.7 \pm 0.1$ ms^{-1} reported for the quiet sun $|B| < 1$ G bins in top right panel Figure 12. That velocities are quite similar to quiet sun conditions is not surprising because this current-channel footpoint region contains weak magnetic field ranging from -24 to 24 G. The weak field has already been discussed as an inconsistency between the photospheric observations and the simplified flux-rope geometry which should have strong magnetic field in the current channel. Although, the absolute Doppler velocities are not known, they are bounded. The absolute errors must be much less than the passband of the filter ≈ 7 kms^{-1} and are likely less than 100 ms^{-1} because the average quiet sun is not moving toward the Earth at several kms^{-1} given the agreement for the coefficient L_0 for the MDI Doppler measurements and (Snodgrass 1984). None of the observed Doppler velocities approach magnitudes of 10^3 kms^{-1} which would be consistent with the analysis in Section 3 — these upflows would be too weak to transport the poloidal flux into the corona necessary to drive the CME eruption within the context of the flux-rope model. These data falsify the flux injection mechanism as a driver for this CME. However, an interesting feature is the sharp decrease of roughly 50 ms^{-1} peak to minimum in the redshift of the left prominence channel (solid red) beginning just after the GOES X-ray flux begins to rise and lasting 1 hr and 35 minutes bounded by the two vertical lines. The flow velocity then appears to recover to its initial value over the next $2\frac{1}{2}$ hr. Through this dynamic change of Doppler velocity in the filament channel, the magnitude remains redshifted 100 ms^{-1} relative to the quiet sun. To determine if dynamic change in the Doppler velocity of filament footpoints is a common characteristic of filament eruptions producing CMEs will require evaluating more events.

5. COMPARISON WITH PREVIOUS WORK AND CONCLUSIONS

The flux-injection hypothesis requires a large energy transport of 2×10^{33} erg across the photosphere on timescales of 600-1200 s. If this hypothesis is correct, then the absence of any significant photospheric signature of this transport is certainly surprising given that the power requirements $\simeq 3 \times 10^{30}$ ergs^{-1} exceed that of the typical solar flare $\lesssim 10^{29}$ ergs^{-1} . Sudol & Harvey (2005) and Fletcher & Hudson (2008) have observed permanent changes in longitudinal magnetograms concomitant with solar flares, and a more comprehensive follow-on study by Petrie & Sudol (2009) has demonstrated that these changes are associated with every flare. However, these changes *always* lag the rise of the flare and thus would lag the peak in the CME acceleration which is strongly correlated with the flare rise time (Shanmugaraju et al. 2003; Zhang et al. 2001, 2004). Furthermore, the changes in the longitudinal magnetograms are largest for events near the limb suggesting that they are caused by a rapid change in the angle of the magnetic field through the

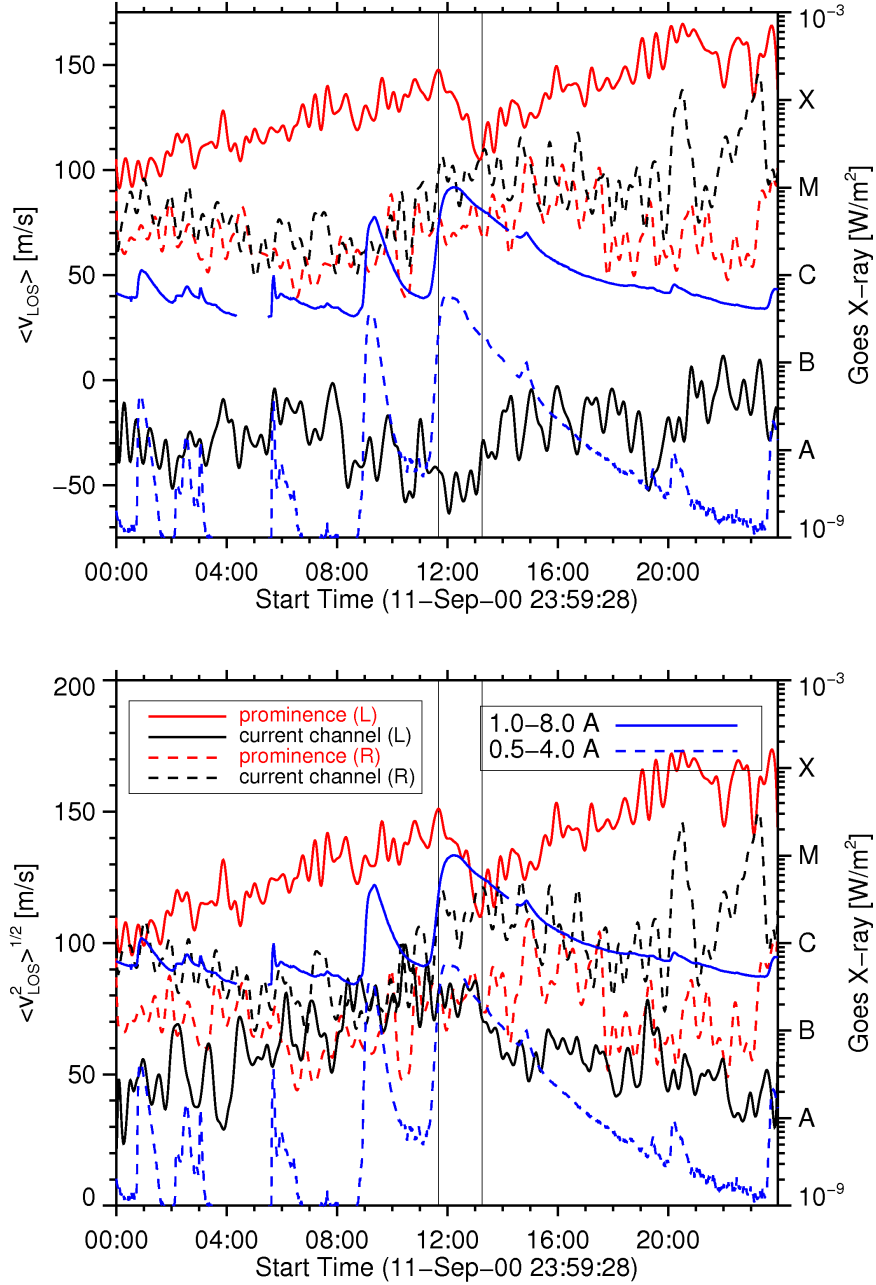


Fig. 14.— Line-of-sight velocity (top) and the rms line of sight velocity (bottom) averaged over the current channel of radius $a_p = 6.7 \times 10^8$ cm for the filament channel (red) and current channels (black) on the left (solid) and right (dashed) and the soft X-ray flux observed by GOES 8 (blue).

photosphere rather than a true change in photospheric magnetic field strength.

The present study has failed to find evidence of the magnetized photospheric plasma velocities required

for the flux-injection hypothesis to satisfy the CME energy budget on timescales of the eruption. Chen et al. (2000), Chen (2001), Krall et al. (2001), Chen & Krall (2003) and Chen & Kunkel (2010) have attempted to address the criticisms of the flux-injection hypothesis based on energy arguments. Chen et al. (2000) cite one-dimensional simulations by Huba & Chen (1996) of a step function horizontal magnetic field of tens of Gauss injected into the low chromosphere. The unspecified current system generating and maintaining the magnetic piston is assumed to lie below the simulation boundary in the photosphere—this is a different situation than the diagrams in Figures 1 and 2. The simulation does not include the photosphere (J. Huba, personal communication 2008 December) and the plasma and neutrals only attain vertical velocities of $v_\zeta \simeq$ tens of m s^{-1} in the low chromosphere. Chen et al. (2000) infer that these simulations imply photospheric upflow velocities of *merely meters per second*. Can these results be used to satisfy the power requirements of the flux-rope model? Assuming a constant horizontal magnetic field $B_h \simeq 30$ G over a large area $\pi (S_f/2)^2 = 2 \times 10^{21} \text{ cm}^2$ surrounding each current channel and a vertical plasma velocity of $v_\zeta = 10 \text{ m s}^{-1}$, the power supplied by this one-dimensional simulation over two footpoints would be $dU_\theta/dt \simeq v_\zeta B_h^2 (S_f/2)^2 / 2 = 8 \times 10^{26} \text{ erg s}^{-1}$ which is *still* more than 2 orders of magnitude less than the power requirements of the 2000 September 12 CME (Chen et al. 2006; Chen & Kunkel 2010) which was associated with an M1.0 flare and more than 3 orders of magnitude less than the power requirements of the 2003 October 28 CME which was associated with an X17 flare (Krall et al. 2006).

Krall et al. (2000) consider the constraints of driving the flux-rope model by footpoint twisting. They conclude that footpoint twisting is inefficient and cannot reproduce the characteristics of the CME trajectories event with large photospheric poloidal velocities of 10 km s^{-1} . However, this estimate corresponds to velocities at the base of the corona based on their values of current-channel radius, and poloidal and toroidal magnetic field (see Eqs (31-33) and Tables 1 and 2 in Krall et al. 2000). They coupled footpoint twisting to the flux-rope model by relating *net* current and poloidal magnetic field at the edge of the current channel to the number of twists at the base of the corona. However, footpoint twisting merely rearranges the current distribution in the current channel leaving the net current constant. Footpoint twisting should be coupled to the flux-rope model through the change in internal inductance as outlined in Appendix C not by modifying the net current and poloidal magnetic field at the edge of the current channel.

Krall et al. (2001) argue that the flux-injection hypothesis implies radial plasma velocities of the order of $v_r \simeq 1 \text{ km s}^{-1}$ at the footpoints of the flux rope implied by the inductive toroidal electric field $E_\phi \simeq -c^{-1} \partial_t A_\phi$. These velocities are already substantial and should be well within the observational capabilities of MDI aboard *SOHO* and ground based observatories. However, this electric field is not relevant to estimating the Poynting flux because $\mathbf{E}_\phi \times \mathbf{B} \simeq (B_\theta/c) \partial_t A_\phi \hat{r}$ is roughly tangent to the photosphere—the vertical Poynting flux is zero (see Figure 2 for the geometry). Similarly the vertical helicity flux $\mathbf{E} \times \mathbf{A}_R$ is also zero for the toroidal electric field.

Chen & Krall (2003) have argued that the photospheric velocities should be highly nonuniform with coherence scales of less than $\sim 10^5$ km consistent with a high $\beta \gg 1$ plasma outside the current channel although no theoretical estimate of this coherence length has been provided. High-resolution convection simulations exhibit rms fluctuations in the $\tau = 1$ surface of ≈ 30 km which is much less than the local photospheric pressure scale height,¹¹ casting doubt upon these assertions. Although the region far from the current channel is $\beta \gg 1$, the region containing the toroidal field and toroidal currents is $\beta \simeq 1$. Section 3 has demonstrated that a significant amount of poloidal energy is injected in the region very near and interior to the current channel $r \leq 2 a_p$. Finally, the spatial scale of the $10'' \text{ pixel}^{-1}$ for MDI corresponds to $\simeq 7500$ km.

¹¹B. Abbett, personnel communication 2009 July.

The photospheric dynamics detected at this scale concomitant with the eruption at the footpoints of the 2000 September 12 CME are not sufficient to drive the eruption.

Emerging horizontal magnetic fields will carry mass into the chromosphere. For velocities much less than the escape velocity $v_{\odot} = 617 \text{ km s}^{-1}$ this mass will flow downward as the magnetic field at the footpoints of the forming loops become more vertically inclined. Indeed, Ishikawa et al. (2008) have observed a strongly redshifted $+5 \text{ km s}^{-1}$ Stokes V profile (downflows) at one end of an emerging horizontal magnetic feature. However, the turbulence argument of Chen & Krall (2003) does not seem to appreciate the very large and continuous *average* velocities \simeq hundreds of km s^{-1} necessary to satisfy the power budget of the flux-rope model. In the limit $v_{\theta_p} = 0$, the *average* vertical velocities in the current channel exceed the escape velocity v_{\odot} and the mass could only be restrained by magnetic forces. The expected velocities also exceed the Alfvén V_A and sound speed C_s in an ideal MHD plasma. Furthermore, regions of downflow embedded in the upflow would imply *larger* upflow velocities to enhance vertical transport to account for the smaller effective upflow area and to balance any energy transported out of the corona through the photosphere in the downflow regions (unless downflow regions are assumed special and contain no horizontal field).

In a similar vein Krall et al. (2001) and Chen & Krall (2003) have argued that filling factor f —the percentage of a pixel that contains magnetized atmosphere—in the photosphere is unknown and the inherent nonuniformity of the magnetic field in the photosphere explains the lack of observational evidence for flux injection. However, the filling factor can in principle be estimated by modern magnetographs by enforcing consistency between the Stokes I profile and the Q (linear), U (linear), and V (circular polarization) profiles (Keppens & Martinez Pillet 1996). Indeed, the filling factor will be a standard data product of the next generation vector magnetograms produced by *SDO/HMI*. The non-magnetic component only contributes to the Stokes I profile, whereas the Doppler velocities are usually determined from the V profile providing a relatively unambiguous estimate for the velocity of the *magnetized* atmosphere. Although Stokes V spectra may exhibit features of both upflows and downflows simultaneously (Bellot Rubio et al. 2001), the observations in Section 4 require precise cancellation between the upflows and downflows to produce no evidence of significant dynamics in the flux-rope footpoint regions necessary for consistency with the flux-injection hypothesis. This perfect cancellation seems improbable.

The large photospheric velocities implied by the flux-rope model power budget would shift the spectral lines used to estimate the magnetic field and Doppler velocity out of the pass-band of many modern telescopes. For example, the MDI instrument records filtergrams around the Ni I spectral line Ni I 6767.8 Å with a 94 mÅ bandpass. Under normal operation, filtergrams are made at five tuning positions separated by 75 mÅ spanning 377 mÅ (Scherrer et al. 1995). The maximum velocity that could be measured by the MDI instrument is $v = c \Delta\lambda/\lambda = 0.150/6767.8 \approx 7 \text{ km s}^{-1}$. The absence of significant changes in the magnetic field indicate that a large fraction of the magnetized atmosphere *is not* moving with velocities that exceed 5 km s^{-1} .

A simple photospheric magnetic field model for flux-rope footpoints has been developed by extrapolating the flux-rope magnetic field model of Chen & Garren (1994), Chen (1996), Krall et al. (2000), and Krall & Chen (2005) into the photosphere with conservation of toroidal flux and toroidal current. This is equivalent to magnetic field models implemented in simulation studies of photospheric flux injection (Chen & Huba 2005a,b, 2006). This magnetic field model has been used to estimate the minimum photospheric velocities necessary to satisfy the power budget of the flux-rope model for CMEs fitted by Chen et al. (2006), Krall et al. (2006), and (Chen & Kunkel 2010). The flux-rope power budget requires large average poloidal or vertical velocities of the order of *hundreds to thousands of km s^{-1}* over large photospheric areas of 10^8 km^2 to transport the necessary poloidal magnetic field into the corona on a timescale of the eruption. While

Chen, Krall, and Kunkel might argue that the photospheric magnetic field implemented in this study is oversimplified, there is agreement that enhanced photospheric activity should be detected in the region near the footpoints. Indeed, Krall et al. (2001) affirm “with certainty we can state that flux injection as discussed above should be accompanied by increased photospheric flow activity over a large spatial area, near the footpoints, for a period of hours during and following a CME eruption.” To address this, Doppler and magnetic field observations at the footpoints of the 2000 September 12 CME have been analyzed. No significant dynamics at the flux-rope current-channel footpoints concomitant with the CME eruption have been detected. The flux-injection hypothesis is incompatible with these observations.

Although, the flux-injection hypothesis has been falsified, the flux-rope model (Chen 1989, 1996) could remain a useful theoretical tool for modeling and interpreting CME dynamics because there are other hypotheses for forming or increasing the poloidal flux of a flux rope. For example, shearing (Mikić & Linker 1994; Antiochos et al. 1999; Amari et al. 2000), converging flows (Forbes & Priest 1995), or nearby emerging flux (Chen & Shibata 2000) may convert coronal arcade field into flux-rope fields via rapid reconnection.¹² Consequently, the flux-injection hypothesis is incorrect, but the flux-rope model could correctly describe the dynamics of an erupting CME. Finally, the flux-rope model has brought to the forefront, the paradigm that CMEs are current carrying coherent magnetic structures consistent with the three-part morphology observed by LASCO coronagraphs and predicts the scaling law that height of the CME at maximum acceleration scales with the footpoint separation distance S_f (Chen et al. 2006).

While the focus of this investigation has been the flux-injection hypothesis (Chen et al. 1997, 2000; Wood et al. 1999; Krall et al. 2001; Chen & Krall 2003; Chen et al. 2006; Krall et al. 2006; Chen & Kunkel 2010), the observational component of this study places important constraints on any hypothesis that relies on the photosphere for the power $10^{29} - 10^{30} \text{ erg s}^{-1}$ driving a CME. These hypotheses are likely incompatible with the present investigation, because the small velocities observed in the photosphere cannot supply the necessary energy on the timescale of the main acceleration phase of the CME. In contrast, the storage-release mechanism, where the energy is transported across the photosphere over a period of hours or days and then released rapidly through reconnection, is compatible with the present study. Under storage release, the power supplied by reconnection is limited by the reconnection rate, in part, determined by the velocity of the reconnection point as it unzips the overlying arcade.

The author thanks the reviewer for his/her constructive criticism that greatly clarified and improved the paper. The author gratefully acknowledges insightful conversations with Jonathan Krall, Joseph Huba, Mark Linton, K. D. Leka, Todd Hoekesema, Werner Poetzi, and Uri Feldman. The author thanks the *SOHO/SOI* team for providing the Dopplergrams and magnetograms.

A. THE MINIMUM PHOTOSPHERIC VELOCITIES CONSISTENT WITH THE POWER BUDGET

The minimum photospheric velocities consistent with the power requirements of the flux-injection hypothesis may be found from a constrained variational principle where

$$\mathcal{I}_1 = \int_0^{r_c} dr r v_\theta^2, \quad (\text{A1})$$

¹²Falsification of one hypothesis does not imply verification of another.

$$\mathcal{I}_2 = \int_0^{r_c} dr r v_\zeta^2, \quad (\text{A2})$$

or

$$\mathcal{I}_3 = \int_0^{r_c} dr r (v_\theta^2 + v_\zeta^2), \quad (\text{A3})$$

is minimized subject to the integral constraint

$$\mathcal{C}_1 \equiv \frac{dU_\theta}{dt} = - \int_0^{r_c} dr r B_\theta(r) \psi'(r), \quad (\text{A4})$$

where $\psi'(r) = \partial_r \psi$. This leads to the functional

$$\mathcal{H} \equiv [\psi'(r)]^2 f^2(r) - \lambda B_\theta(r) \psi'(r), \quad (\text{A5})$$

and the Euler equation

$$\frac{\partial \mathcal{H}}{\partial \psi'} = \kappa = \text{constant}, \quad (\text{A6})$$

where λ is a Lagrange multiplier. There are two limiting cases and a third general case to consider:

Case 1: $v_\parallel \neq 0$, $v_\zeta = 0$, and $f = B_\zeta^{-1}$.

Solving for ψ'

$$\psi' = \frac{B_\zeta^2}{2} (\kappa_1 + \lambda B_\theta), \quad (\text{A7a})$$

$$v_\theta = \frac{B_\zeta}{2} (\kappa_1 + \lambda B_\theta). \quad (\text{A7b})$$

Physical considerations require $v_\theta \rightarrow 0$ when $r \rightarrow 0$ which is equivalent to $B_\theta \rightarrow 0$. This implies $\kappa_1 \equiv 0$ and

$$\psi' = \frac{\lambda}{2} B_\theta B_\zeta^2, \quad (\text{A8a})$$

$$v_\theta = \frac{\lambda}{2} B_\theta B_\zeta. \quad (\text{A8b})$$

Substituting Equation (A8a) into Equation (A4) determines the Lagrange multiplier

$$\lambda \equiv - \frac{1120 \mathcal{C}_1}{437 B_{\zeta p}^2 B_{\theta p}^2 a_p^2}. \quad (\text{A9})$$

Substituting Equations (A9) and Equation (A8b) into (A1), integrating from $r = 0 \Rightarrow a_p$ and using Equations (14a) and (14b) the rms poloidal plasma velocity inside $r \leq a_p$ is

$$\langle v_\theta^2 \rangle_{a_p}^{1/2} = \left| \frac{dU_\theta}{dt} \right| \frac{4 \sqrt{70}}{\sqrt{437 |B_{\theta c}^2 B_{\zeta c}| a_c^2}} \frac{1}{\sqrt{|B_{\zeta p}|}}. \quad (\text{A10})$$

Case 2: $v_\parallel \neq 0$, $v_\theta = 0$, and $f = B_\theta^{-1}$

Solving for ψ'

$$\psi' = \frac{B_\theta^2}{2} (\kappa_2 + \lambda B_\theta), \quad (\text{A11a})$$

$$v_\zeta = - \frac{B_\theta}{2} (\kappa_2 + \lambda B_\theta). \quad (\text{A11b})$$

The Lagrange multiplier is determined by substituting Equation (A11a) into Equation (A4)

$$\lambda \equiv - \frac{6 r_c \left(85085 B_{\theta p}^3 a_p^3 \kappa_2 - 170170 \mathcal{C}_1 r_c - 144048 B_{\theta p}^3 a_p^2 r_c \kappa_2 \right)}{221 B_{\theta p}^4 a_p^2 \left(1155 a_p^2 - 2998 r_c^2 \right)}. \quad (\text{A12})$$

Substituting Equations (A12) and (A11b) into Equation (A2), differentiating with respect to κ_2 , and solving determines the value of $\kappa_2 = 0$ corresponding to the minimum mean squared velocity over the region $r = 0 \rightarrow r_c$. Integrating Equation (A2) from $r = 0 \rightarrow 2 a_p$ with Equations (14a) and (14b) produces the rms vertical velocity inside $r \leq 2 a_p$

$$\langle v_\zeta^2 \rangle_{2 a_p}^{1/2} = \left| \frac{dU_\theta}{dt} \right| \frac{\sqrt{12516735} |B_{\zeta p}| r_c^2}{2 B_{\theta c}^2 a_c^2 |2998 B_{\zeta p} r_c^2 - 1155 B_{\zeta c} a_c^2|}. \quad (\text{A13})$$

Case 3: $v_{\parallel} = 0$, $f = 1/\sqrt{B_\theta^2 + B_\zeta^2}$

Solving for ψ'

$$\psi' = \frac{B_\theta^2 + B_\zeta^2}{2} (\kappa_3 + \lambda B_\theta), \quad (\text{A14a})$$

$$\mathbf{v} = \frac{(\kappa_3 + \lambda B_\theta)}{2} (0, B_\zeta, -B_\theta). \quad (\text{A14b})$$

Physical considerations require $v_\theta \rightarrow 0$ when $r \rightarrow 0$ which is equivalent to $B_\theta \rightarrow 0$. This implies $\kappa_3 \equiv 0$ and

$$\psi' = \frac{\lambda B_\theta}{2} (B_\theta^2 + B_\zeta^2), \quad (\text{A15a})$$

$$\mathbf{v} = \frac{\lambda B_\theta}{2} (0, B_\zeta, -B_\theta). \quad (\text{A15b})$$

Substituting Equation (A15a) into Equation (A4) determines the Lagrange multiplier

$$\lambda \equiv \frac{36960 \mathcal{C}_1 r_c^2}{9240 a_p^4 B_{\theta p}^4 - a_p^2 B_{\theta p}^2 \left(23984 B_{\theta p}^2 + 14421 B_{\zeta p}^2 \right) r_c^2}, \quad (\text{A16})$$

Substituting Equations (A16) and (A15b) into Equation (A3), integrating from $r = 0 \Rightarrow a_p$ and using Equations (14a) and (14b) the rms total plasma velocity inside $r \leq a_p$ is

$$\langle v^2 \rangle_{2 a_p}^{1/2} = \left| \frac{dU_\theta}{dt} \right| \frac{2 B_{\zeta p} r_c^2 \sqrt{2310} \sqrt{21674 B_{\theta c}^2 + 14421 B_{\zeta c} B_{\zeta p}}}{a_c^2 |B_{\theta c} B_{\zeta p} (23984 B_{\theta c}^2 + 14421 B_{\zeta c} B_{\zeta p}) r_c^2 - 9240 a_c^4 B_{\theta c}^3 B_{\zeta c}|}, \quad (\text{A17a})$$

the poloidal plasma velocity is

$$\langle v_\theta^2 \rangle_{2 a_p}^{1/2} = \left| \frac{dU_\theta}{dt} \right| \frac{66 r_c^2 \sqrt{30590} |B_{\zeta c} B_{\zeta p}^3|}{a_c^2 |B_{\theta c} B_{\zeta p} (23984 B_{\theta c}^2 + 14421 B_{\zeta c} B_{\zeta p}) r_c^2 - 9240 a_c^4 B_{\theta c}^3 B_{\zeta c}|} \quad (\text{A17b})$$

and the vertical plasma velocity is

$$\langle v_\zeta^2 \rangle_{2 a_p}^{1/2} = \left| \frac{dU_\theta}{dt} \right| \frac{4 B_{\zeta p} r_c^2 \sqrt{12516735}}{a_c^2 |B_{\zeta p} (23984 B_{\theta c}^2 + 14421 B_{\zeta c} B_{\zeta p}) r_c^2 - 9240 a_c^4 B_{\theta c}^2 B_{\zeta c}|}. \quad (\text{A17c})$$

B. THE MINIMUM PHOTOSPHERIC VELOCITIES CONSISTENT WITH THE HELICITY BUDGET

The vector potential in the upper half plane ($z \geq 0$) for an azimuthally symmetric vertical magnetic field is

$$\mathbf{A}_R(r, z) = \frac{2 J_1(\gamma_n r) e^{-\gamma_n \zeta} \int_0^a dr r J_0(\gamma_n r) B_\zeta(r)}{\alpha_n a J_1^2(\alpha_n)} \hat{\theta} \quad (\text{B1})$$

where $\alpha_{n=1,2,\dots} = 2.40483, 5.52008, \dots$ is the n th zero of the zeroth-order Bessel function $J_0(\alpha_n) = 0$. This potential field satisfies

$$\nabla \cdot \mathbf{A}_R(r, \zeta) = 0, \quad (\text{B2a})$$

$$\hat{n} \cdot \mathbf{A}_R(r, 0) = 0, \quad (\text{B2b})$$

$$\mathbf{B}_R(r, \zeta) = \nabla \times \mathbf{A}_R(r, \zeta) = \nabla \Psi_R(r, \zeta), \quad (\text{B2c})$$

$$\hat{n} \cdot \mathbf{B}_R(r, 0) = B_\zeta(r). \quad (\text{B2d})$$

$$\mathbf{A}_R(r, 0) = \frac{a B_{\zeta a}}{2} \hat{\theta} \begin{cases} 3 \frac{r}{a} \left(1 - \frac{r^2}{a^2} + \frac{r^4}{3a^4} \right) & r \leq a, \\ \frac{a}{r} & r > a. \end{cases} \quad (\text{B3})$$

$$\mathcal{C}_2 \equiv \frac{d\Delta K}{dt} = -8\pi \int_0^{r_c} dr r A_{\theta R}(r) \psi'(r). \quad (\text{B4})$$

The minimum photospheric velocities consistent with the helicity budget may be found by following the procedure outlined in Appendix A using Equation (A5) with $B_\theta \implies A_{\theta R}$.

$$\mathcal{H} \equiv [\psi'(r)]^2 f^2(r) - \lambda A_{\theta R}(r) \psi'(r). \quad (\text{B5})$$

Case 1: $v_{\parallel} \neq 0$, $v_\zeta = 0$, and $f = B_\zeta^{-1}$.

$$\lambda \equiv -\frac{560 \mathcal{C}_2}{437 \pi a_p^4 B_{\zeta p}^4} \quad (\text{B6})$$

$$\langle v_\zeta^2 \rangle_{2a_p}^{1/2} = \left| \frac{d\Phi_\theta}{dt} \right| \frac{\sqrt{1155 |B_{\zeta c}|}}{2 B_{\theta c} \sqrt{|2998 B_{\zeta p} r_c^2 - 1155 B_{\zeta c} a_c^2|}}. \quad (\text{B7})$$

Case 2: $v_{\parallel} \neq 0$, $v_\theta = 0$, and $f = B_\theta^{-1}$

$$\lambda \equiv \frac{2310 r_c^2 \mathcal{C}_2}{B_{\theta p}^2 B_{\zeta p}^2 \pi a_p^4 (2998 r_c^2 - 1155 a_p^2)} \quad (\text{B8})$$

$$\langle v_\zeta^2 \rangle_{2a_p}^{1/2} = \left| \frac{d\Phi_\theta}{dt} \right| \frac{\sqrt{1155 |B_{\zeta c}|}}{2 B_{\theta c} \sqrt{|2998 B_{\zeta p} r_c^2 - 1155 B_{\zeta c} a_c^2|}}. \quad (\text{B9})$$

Case 3: $v_{\parallel} = 0$ and $f = 1/\sqrt{B_\theta^2 + B_\zeta^2}$

$$\lambda \equiv -\frac{18480 \mathcal{C}_2 r_c^2}{B_{\zeta p}^2 \pi a_p^4 \left[(23984 B_{\theta p}^2 + 14421 B_{\zeta p}^2) r_c^2 - 9240 B_{\theta p}^2 a_p^2 \right]}, \quad (\text{B10})$$

$$\langle v^2 \rangle_{2a_p}^{1/2} = \left| \frac{d\Phi_\theta}{dt} \right| \frac{B_{\zeta p} r_c^2 \sqrt{2310} \sqrt{21674 B_{\theta c}^2 + 14421 B_{\zeta c} B_{\zeta p}}}{2 a_c |B_{\zeta p} (23984 B_{\theta c}^2 + 14421 B_{\zeta c} B_{\zeta p}) r_c^2 - 9240 a_c^4 B_{\theta c}^2 B_{\zeta c}|}, \quad (\text{B11})$$

C. ROTATIONAL TRANSFORM

Krall et al. (2000) assert that footpoint twisting modifies the *net* current and poloidal magnetic field at the edge of the current channel based on a geometrical argument. Generally, the twist of a flux rope is estimated from the field line equations

$$\frac{dr}{B_r} = \frac{r d\theta}{B_\theta(r)} = \frac{\mathcal{R} d\phi}{B_\phi(r)}. \quad (\text{C1})$$

For a circular torus, the amount of rotation of the poloidal field about the toroidal axis during the transit along the flux rope above the photosphere is estimated from the rotational transform (effectively the reciprocal of the safety factor calculation for Tokamaks)

$$\Delta\theta(r) \simeq \int_0^{2\pi\Theta} d\phi \frac{\mathcal{R} B_\theta(r)}{r B_\phi(r)}, \quad (\text{C2a})$$

$$\simeq 2\pi\Theta \frac{\mathcal{R} B_\theta(r)}{r B_\phi(r)} \quad (\text{C2b})$$

The amount of twist is a function of minor radius r . To add an amount of twist $\delta\vartheta(r)$ to the flux rope, the equation becomes

$$\Delta\theta(r) + \delta\vartheta(r) = 2\pi\Theta \frac{\mathcal{R} B_\theta(r)}{r B_\phi(r)} + \delta\vartheta(r) = 2\pi\Theta \frac{\mathcal{R} \tilde{B}_\theta(r)}{r B_\phi(r)} \quad (\text{C3})$$

where B_θ is the initial poloidal field and

$$\tilde{B}_\theta(r) = B_\theta(r) + \frac{\delta\vartheta(r)}{2\pi\Theta} \frac{r}{\mathcal{R}} B_\phi(r), \quad (\text{C4})$$

\tilde{B}_θ is the final poloidal field. This equation has a similar form to Equation (31) in Krall et al. (2000)

$$\tilde{B}_{\theta c} = B_{\theta c} + \frac{\delta\vartheta_0}{2\pi\Theta} \frac{a_c}{\mathcal{R}} B_{\phi c}, \quad (\text{C5})$$

where $\delta\vartheta_0 = \pi$ is a uniform twist. However, there are important mathematical and conceptual differences between Equations (C4) and (C5). The former Equation (C4) implies that the *poloidal magnetic field profile* changes as a result of the twist whereas the latter Equation (C5) relates the coefficient of Equation (9a) before and after the twist. Krall et al. (2000) substitute Equation (9a) into effectively Equation (10b) to produce a new current

$$\tilde{I}_\phi = \frac{a_c c}{2} \tilde{B}_{\theta c} = \frac{a_c c}{2} \left(B_{\theta c} + \frac{\delta\vartheta_0}{2\pi\Theta} \frac{a_c}{\mathcal{R}} B_{\phi c} \right), \quad (\text{C6})$$

where $\delta\vartheta_0 = v_{\theta_0} t$. However, the correct relationship Equation (C4) implies that $\tilde{B}_\theta(a) = B_\theta(a)$ and $\tilde{I}_\phi = I_\phi = B_\theta(a) a_c c/2$ because $B_\phi(a) = 0$, i.e., there is no change in net current as a consequence of the twisting! The effect of twisting is to modify the current distribution in the current channel and change the internal inductance

$$\tilde{\xi} \equiv \frac{2 \int_0^a dr r \tilde{B}_\theta^2(r)}{a^2 B_{\theta a}^2}. \quad (\text{C7})$$

REFERENCES

- Abbett, W. P., Fisher, G. H., Fan, Y., & Bercik, D. J. 2004, *ApJ*, 612, 557
- Amari, T., Luciani, J. F., Mikić, Z., & Linker, J. 2000, *ApJ*, 529, L49
- Antiochos, S. K., DeVore, C. R., & Klimchuk, J. A. 1999, *ApJ*, 510, 485
- Bellot Rubio, L. R., Rodríguez Hidalgo, I., Collados, M., Khomenko, E., & Ruiz Cobo, B. 2001, *ApJ*, 560, 1010
- Berger, M. A., & Field, G. B. 1984, *Journal of Fluid Mechanics*, 147
- Bieber, J. W., Clem, J., Evenson, P., Pyle, R., Ruffolo, D., & Sáiz, A. 2005, *Geophys. Res. Lett.*, 32, 3
- Brueckner, G. E., Howard, R. A., Koomen, M. J., Korendyke, C. M., Michels, D. J., Moses, J. D., Socker, D. G., Dere, K. P., Lamy, P. L., Llebaria, A., Bout, M. V., Schwenn, R., Simnett, G. M., Bedford, D. K., & Eyles, C. J. 1995, *Sol. Phys.*, 162, 357
- Bruls, J. H. M. J. 1993, *A&A*, 269, 509
- Bumba, V., & Klvaňa, M. 1995, *Sol. Phys.*, 160, 245
- Butterworth, S. 1930, *Experimental Wireless and the Wireless Engineer*
- Chen, J. 1989, *ApJ*, 338, 453
- 1996, *J. Geophys. Res.*, 101, 27499
- 1997, *Prominence Eruptions and Geoeffective Solar Wind Structures (Magnetic Storms, Geophysical Monograph Series, Vol. 98)*, 45–+
- 2001, *Space Science Reviews*, 95, 165
- 2007, *Physical Review Letters*, 99, 099501
- Chen, J., & Garren, D. A. 1993, *Geophys. Res. Lett.*, 20, 2319
- Chen, J., & Garren, D. A. 1994, in *ESA Special Publication, Vol. 373, Solar Dynamic Phenomena and Solar Wind Consequences, the Third SOHO Workshop*, ed. J. J. Hunt, 285–+
- Chen, J., Howard, R. A., Brueckner, G. E., Santoro, R., Krall, J., Paswaters, S. E., St. Cyr, O. C., Schwenn, R., Lamy, P., & Simnett, G. M. 1997, *ApJ*, 490, L191+
- Chen, J., & Huba, J. D. 2005a, *AGU Fall Meeting Abstracts*, A269+
- 2005b, *AGU Spring Meeting Abstracts*, B8+
- Chen, J., & Huba, J. D. 2006, in *Bulletin of the American Astronomical Society, Vol. 38, Bulletin of the American Astronomical Society*, 228–+
- Chen, J., & Krall, J. 2003, *Journal of Geophysical Research (Space Physics)*, 108, 1410
- 2004, *AGU Fall Meeting Abstracts*, A8+
- Chen, J., & Kunkel, V. 2010, Submitted to *Astrophys. J.*

- Chen, J., Marqué, C., Vourlidas, A., Krall, J., & Schuck, P. W. 2006, *ApJ*, 649, 452
- Chen, J., Santoro, R. A., Krall, J., Howard, R. A., Duffin, R., Moses, J. D., Brueckner, G. E., Darnell, J. A., & Burkepille, J. T. 2000, *ApJ*, 533, 481
- Chen, J., Schuck, P., & Kunkel, V. 2008, 2008 NRL Review (Washington, DC: Naval Research Laboratory), 231–233
- Chen, P. F., & Shibata, K. 2000, *ApJ*, 545, 524
- Chi, P. J., Russell, C. T., Foster, J. C., Moldwin, M. B., Engebretson, M. J., & Mann, I. R. 2005, *Geophys. Res. Lett.*, 32, 3
- Craven, P., & Wahba, G. 1979, *Numerische Mathematik*, 31, 377
- Degenstein, D. A., Lloyd, N. D., Bourassa, A. E., Gattinger, R. L., & Llewellyn, E. J. 2005, *Geophys. Res. Lett.*, 32, 3
- Delaboudinière, J., Artzner, G. E., Brunaud, J., Gabriel, A. H., Hochedez, J. F., Millier, F., Song, X. Y., Au, B., Dere, K. P., Howard, R. A., Kreplin, R., Michels, D. J., Moses, J. D., Defise, J. M., Jamar, C., Rochus, P., Chauvineau, J. P., Marioge, J. P., Catura, R. C., Lemen, J. R., Shing, L., Stern, R. A., Gurman, J. B., Neupert, W. M., Maucherat, A., Clette, F., Cugnon, P., & van Dessel, E. L. 1995, *Sol. Phys.*, 162, 291
- Dravins, D. 1982, *ARA&A*, 20, 61
- Finn, J., & Antonsen, T. 1985, *Comments Plasma Phys. Controlled Fusion*, 9, 111
- Fletcher, L., & Hudson, H. S. 2008, *ApJ*, 675, 1645
- Forbes, T. G. 2000, *J. Geophys. Res.*, 105, 23153
- . 2001, AGU Spring Meeting Abstracts, 41
- Forbes, T. G., & Priest, E. R. 1995, *ApJ*, 446, 377
- Gopalswamy, N., Barbieri, L., Lu, G., Plunkett, S. P., & Skoug, R. M. 2005, *Geophys. Res. Lett.*, 32, 3
- Harra, L. K., Hara, H., Imada, S., Young, P. R., Williams, D. R., Sterling, A. C., Korendyke, C., & Attrill, G. D. R. 2007, *PASJ*, 59, 801
- Hathaway, D. H. 1992, *Sol. Phys.*, 137, 15
- Hathaway, D. H., Beck, J. G., Bogart, R. S., Bachmann, K. T., Khatri, G., Petitto, J. M., Han, S., & Raymond, J. 2000, *Sol. Phys.*, 193, 299
- Hu, Q., Smith, C. W., Ness, N. F., & Skoug, R. M. 2005, *Journal of Geophysical Research (Space Physics)*, 110, 9
- Huba, J. D., & Chen, J. 1996, *ApJ*, 469, 412
- Imada, S., Hara, H., Watanabe, T., Kamio, S., Asai, A., Matsuzaki, K., Harra, L. K., & Mariska, J. T. 2007, *PASJ*, 59, 793

- Ishikawa, R., Tsuneta, S., Ichimoto, K., Isobe, H., Katsukawa, Y., Lites, B. W., Nagata, S., Shimizu, T., Shine, R. A., Suematsu, Y., Tarbell, T. D., & Title, A. M. 2008, *A&A*, 481, L25
- Jones, H. P. 1989, *Sol. Phys.*, 120, 211
- Keppens, R., & Martinez Pillet, V. 1996, *A&A*, 316, 229
- Kosovichev, A. G., T. L. Duvall, J., & Scherrer, P. H. 1996, Simulation of Vector-Weighted Binning for the Medium-1 Program, Tech. Rep. SOI-TN-96-130, Stanford University, Stanford, CA
- Krall, J., & Chen, J. 2005, *ApJ*, 628, 1046
- Krall, J., Chen, J., Duffin, R. T., Howard, R. A., & Thompson, B. J. 2001, *ApJ*, 562, 1045
- Krall, J., Chen, J., & Santoro, R. 2000, *ApJ*, 539, 964
- Krall, J., Yurchyshyn, V. B., Slinker, S., Skoug, R. M., & Chen, J. 2006, *ApJ*, 642, 541
- Kusano, K., Maeshiro, T., Yokoyama, T., & Sakurai, T. 2002, *ApJ*, 577, 501
- Landau, L. D., & Lifshitz, E. M. 1960, *Electrodynamics of continuous media* / by L.D. Landau and E.M. Lifshitz ; translated from the Russian by J.B. Skyes and J.S. Bell (Pergamon Press ; Addison-Wesley, Oxford : Reading, Mass. :), ix, 417 p. ;
- Looper, M. D., Blake, J. B., & Mewaldt, R. A. 2005, *Geophys. Res. Lett.*, 32, 3
- Manchester, IV, W. B., Vourlidas, A., Tóth, G., Lugaz, N., Roussev, I. I., Sokolov, I. V., Gombosi, T. I., De Zeeuw, D. L., & Opher, M. 2008, *ApJ*, 684, 1448
- Mikić, Z., & Linker, J. A. 1994, *ApJ*, 430, 898
- Morse, P. M. 1953, *International Series in Pure and Applied Physics, Vol. 1, Methods in Theoretical Physics* (New York: McGraw-Hill Publishing Co.)
- Neidig, D. F. 1989, *Sol. Phys.*, 121, 261
- Pallamraju, D., & Chakrabarti, S. 2005, *Geophys. Res. Lett.*, 32, 3
- Petrie, G., & Sudol, J. J. 2009, in *AAS/Solar Physics Division Meeting, Vol. 41, AAS/Solar Physics Division Meeting*, 862
- Qiu, J., Wang, H., Cheng, C. Z., & Gary, D. E. 2004, *ApJ*, 604, 900
- Régnier, S., Priest, E. R., & Hood, A. W. 2008, *A&A*, 491, 297
- Rust, D. M. 2001, *J. Geophys. Res.*, 106, 25075
- Sakai, J. I., Minamizuka, R., Kawata, T., & Cramer, N. F. 2001, *ApJ*, 550, 1075
- Sakai, J. I., Mizuhata, Y., Kawata, T., & Cramer, N. F. 2000, *The Astrophysical Journal*, 544, 1108
- Scherrer, P. H., Bogart, R. S., Bush, R. I., Hoeksema, J. T., Kosovichev, A. G., Schou, J., Rosenberg, W., Springer, L., Tarbell, T. D., Title, A., Wolfson, C. J., Zayer, I., & MDI Engineering Team. 1995, *Sol. Phys.*, 162, 129

- Schuck, P. W. 2008, *ApJ*, 683, 1134, <http://arxiv.org/abs/0803.3472>
- Schuck, P. W., Chen, J., Schwartz, I. B., & Yurchyshyn, V. 2004b, *ApJ*, 610, 133
- Seppälä, A., Verronen, P. T., Kyrölä, E., Hassinen, S., Backman, L., Hauchecorne, A., Bertaux, J. L., & Fussen, D. 2004, *Geophys. Res. Lett.*, 31, 19107
- Shafranov, V. D. 1966, *Reviews of Plasma Physics*, 2, 103
- Shanmugaraju, A., Moon, Y.-J., Dryer, M., & Umapathy, S. 2003, *Sol. Phys.*, 215, 185
- Skoug, R. M., Gosling, J. T., Steinberg, J. T., McComas, D. J., Smith, C. W., Ness, N. F., Hu, Q., & Burlaga, L. F. 2004, *Journal of Geophysical Research (Space Physics)*, 109, 9102
- Smart, W. M. 1977, *Textbook on Spherical Geometry*, 6th edn. (New York, NY: Cambridge University Press), revised by R. M. Green
- Snodgrass, H. B. 1984, *Sol. Phys.*, 94, 13
- Steinegger, M., Denker, C., Goode, P. R., H. Marquette, W., Varsik, J., Wang, H., Otruba, W., Freislich, H., Hanslmeier, A., Luo, G., Chen, D., & Zhang, W. 2000, in *ESA SP-463: The Solar Cycle and Terrestrial Climate, Solar and Space weather*, 617–622
- Sudol, J. J., & Harvey, J. W. 2005, *ApJ*, 635, 647
- Tran, T., Bertello, L., Ulrich, R. K., & Evans, S. 2005, *ApJS*, 156, 295
- Tsurutani, B. T., Judge, D. L., Guarnieri, F. L., Gangopadhyay, P., Jones, A. R., Nuttall, J., Zambon, G. A., Didkovsky, L., Mannucci, A. J., Iijima, B., Meier, R. R., Immel, T. J., Woods, T. N., Prasad, S., Floyd, L., Huba, J., Solomon, S. C., Straus, P., & Viereck, R. 2005, *Geophys. Res. Lett.*, 32, 3
- Ulrich, R. K., Bertello, L., Boyden, J. E., & Webster, L. 2009, *Sol. Phys.*, 255, 53
- Vernazza, J. E., Avrett, E. H., & Loeser, R. 1981, *ApJS*, 45, 635
- Vršnak, B., Klein, K.-L., Warmuth, A., Otruba, W., & Skender, M. 2003, *Sol. Phys.*, 214, 325
- Welsch, B. T., Abbett, W. P., DeRosa, M. L., Fisher, G. H., Georgoulis, M. K., Kusano, K., Longcope, D. W., Ravindra, B., & Schuck, P. W. 2007, *ApJ*, 670, 1434
- Wheatland, M. S. 2000, *ApJ*, 532, 616
- Woltring, H. J. 1986, *Advances in Engineering Software and Workstations*, 8, 104, 15
- Wood, B. E., Karovska, M., Chen, J., Brueckner, G. E., Cook, J. W., & Howard, R. A. 1999, *ApJ*, 512, 484
- Woods, T. N., Eparvier, F. G., Fontenla, J., Harder, J., Kopp, G., McClintock, W. E., Rottman, G., Smiley, B., & Snow, M. 2004, *Geophys. Res. Lett.*, 31, 10802
- Yurchyshyn, V., Yashiro, S., Abramenko, V., Wang, H., & Gopalswamy, N. 2005, *ApJ*, 619, 599
- Zhang, J., Dere, K. P., Howard, R. A., Kundu, M. R., & White, S. M. 2001, *ApJ*, 559, 452
- Zhang, J., Dere, K. P., Howard, R. A., & Vourlidas, A. 2004, *ApJ*, 604, 420

Zurbuchen, T. H., Gloeckler, G., Ipavich, F., Raines, J., Smith, C. W., & Fisk, L. A. 2004, *Geophys. Res. Lett.*, 31, 11805

Table 1. Fit-determined Coefficients with $\chi^2 = 3898.0$ for a Reduced Set of Disk-orthonormalized Functions Determined from 24 hr of MDI Vector Weighted Dopplergams on 2003 September 12. Estimates $\widehat{\mu}$ and population standard deviations $\widehat{\sigma}_{\mu}$ from Table 2 in Snodgrass (1984) for data taken between 1967 January 1 and 1984 March 5 at the Mount Wilson Solar Observatory.

	$\mu \text{ Rads s}^{-1}$			m s^{-1}							
	A_0	A_2	A_4	L_0	L_1	L_2	L_3	L_4	M_1	M_2	H
$\widehat{\theta}$	3.1870	-0.1610	-0.0216	131	174	88	10	-3.1	-17.4	0.6	29.1
$\widehat{\sigma}_{\theta}$	0.0021	0.0027	0.0027	19	26	21	11	3.5	3.0	0.4	5.0
\widehat{t}_{θ}	1496.81	-59.19	-8.05	6.89	6.64	4.19	0.92	-0.88	-5.76	1.59	5.87
%	0.00	0.00	0.00	0.0	0.0	0.0	35.8	37.7	0.0	11.1	0.0
$\widehat{\mu}$	3.1556	-0.1610	-0.0312	127	160	88	14	2.0	6.2	0.1	8.1
$\widehat{\sigma}_{\mu}$	0.1366	0.0238	0.0136	252	29	24	12	5.4	36.0	8.6	77.1
$\widehat{t}_{\theta\mu}$	0.23	0.00	0.69	0.02	0.34	-0.00	-0.25	-0.79	-0.65	0.06	0.27
%	85.63	99.99	61.49	98.98	78.94	99.92	84.30	57.42	63.10	96.16	83.13